CHALMERS
UNIVERSITY OF TECHNOLOGY

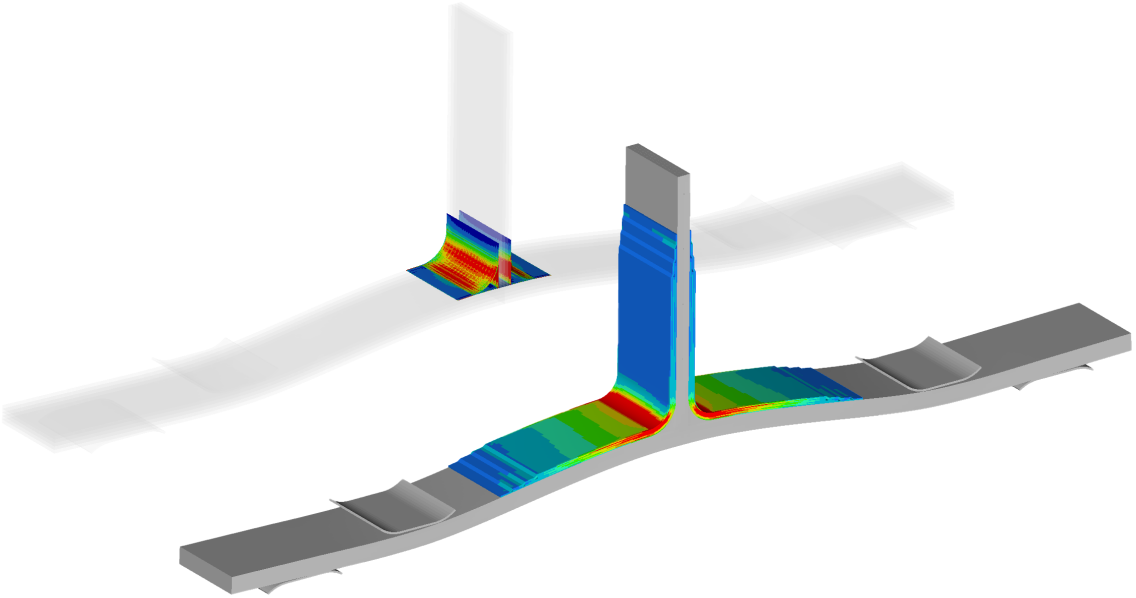

Evaluation and performance analysis of composite pi-joints for structural applications

Master's thesis in Applied Mechanics

GABRIEL PFEIFFER
ANNA WRENNFORS

DEPARTMENT OF INDUSTRIAL AND MATERIALS SCIENCE
CHALMERS UNIVERSITY OF TECHNOLOGY
Gothenburg, Sweden 2025
www.chalmers.se

Master's thesis 2025

Evaluation and performance analysis of composite pi-joints for structural applications

GABRIEL PFEIFFER
ANNA WRENNFORS

CHALMERS
UNIVERSITY OF TECHNOLOGY

Department of Industrial and Materials Science
Division of Material and Computational Mechanics
Chalmers University of Technology
Gothenburg, Sweden 2025

Evaluation and performance analysis of composite pi-joints for structural applications
GABRIEL PFEIFFER
ANNA WRENNFORS

Supervisor: Leandro G Maia, Heart Aerospace
Examiner: Martin Fagerström, Industrial and Materials Science

Master's Thesis 2025
Department of Industrial and Materials Science
Division of Material and Computational Mechanics
Chalmers University of Technology
SE-412 96 Gothenburg
Telephone +46 31 772 1000

Cover: Finite element simulation results (Tsai-wu and cohesive failure) for a composite pi-joint specimen under pull-off loading.

Typeset in LaTeX
Printed by Chalmers Reproservice
Gothenburg, Sweden 2025

Evaluation and performance analysis of composite pi-joints for structural applications

GABRIEL PFEIFFER, ANNA WRENNFORS
Department of Industrial and Material Science
Chalmers University of Technology

Abstract

This thesis investigates and evaluates four types of carbon composite pi-joints for use in structural applications. Two of the four types are designed and manufactured in the thesis using Automated Fibre Placement (AFP) machines and are referred to as L-style and LU-style due to their shape. The other two types are off-the-shelves components, a 3D woven pi-joint from Bally Ribbon Mills, and a braided pi-joint from A&P technology. These configurations are compared based on cost, manufacturing complexity, as well as their predicted strengths calculated using Finite Element (FE) models. These models are developed as part of the thesis to predict the behaviour and failure of the different pi-joints under pull-off and shear load cases.

Additionally, three Non-Destructive Inspections (NDI) methods (X-ray CT-scan, pulse-echo ultrasonic testing (UT) and thermography) are evaluated based on their effectiveness in detecting different types of defects in pi-joints and their scalability for a future production line of aircrafts.

Lastly, all manufacturing processes used for AFP, hot draping and Vacuum Assisted Resin Transfer Moulding (VARTM) are detailed along with a discussion on the challenges encountered. The results show the differences in cost, manufacturability, predicted strengths and the effectiveness of the different NDI methods.

Keywords: composite, pi-joint, structural applications, non-destructive inspection, finite element analysis, manufacturing techniques.

Acknowledgements

We would like to extend a special thanks to Anders Forslund, Waruna Seneviratne, and Upul R. Palliyaguru for making this project possible and for granting us access to state-of-the-art equipment. We also thank Leandro G. Maia, Christopher Boshers, and Ravi Patel for their collaborative efforts and project management. Finally, we are especially grateful to Mohamed Shafie, Ethan McDaniel, and Kyle Tubbs for their valuable technical insights and continuous guidance throughout this work.

Gabriel Pfeiffer, Anna Wrennfors, Gothenburg, August 2025

List of Acronyms

Below is the list of acronyms that have been used throughout this thesis listed in alphabetical order:

AFP	Automated fibre placement
BRM	Bally Ribbon Mills
CT	Computed thermography
CZM	Cohesive zone modelling
FE	Finite Element
FEA	Finite Element Analysis
FOD	Foreign object debris
IR	Infrared
MCS	Material coordinate system
NASA	National Aeronautics and Space Administration
NDI	Non-destructive inspection
PT	Pulsed thermography
TT	Through transmission
UD	Unidirectional
UT	Ultrasonic testing
VARTM	Vacuum assisted resin transfer moulding
VCCT	Virtual Crack Closure Technique
VED	Viscous Energy Dissipation

Contents

List of Figures

List of Tables

1

Introduction

1.1 Background

Over the past century, the commercial aviation industry has significantly advanced in both airframe design and propulsion systems. The wooden airframes of the Wright brothers' era were replaced by riveted metal structures, and later further improved by the composite designs seen in modern aircrafts. Similarly, propulsion systems have progressed from traditional piston engines to turbojet technology, with recent developments focusing on battery-powered electrical propulsion systems, reflecting the industry's commitment to sustainability.

As the aviation industry progresses towards a future of electric regional air travel, minimizing the weight of airframes is becoming increasingly critical to offset the added mass of batteries. One area with potential for weight reduction is the joints between structural components within the wing, such as the interface between spars and wing skins. Traditional designs are based on riveted connections which introduce localized stress concentrations which in turn require additional material to reinforce the joints. Eliminating these riveted connections by using bonded joints, such as composite pi-joints, allows the materials to be used more efficiently, leading to a reduction in overall aircraft weight [34] [9]. However, replacing these conventional joining methods would require significant testing and evaluation.

Early pi-joint research by the National Aeronautics and Space Administration (NASA) for space and high-speed aircraft applications concluded that "bolted joints have weights 2 to 7 times that of corresponding bonded joint" [34]. The project investigated four configurations of bonded and bolted composite joints in varying temperatures and for multiple load cases. The technical report also highlights the added complexity and difficulties to repair these joints if damaged.

The Composites Affordability Initiative, a joint project between multiple US government agencies along with aerospace companies such as Textron, Lockheed Martin, Boeing, and Northrop Grumman investigated the possible potential realized by use of integrated composite structures as well as the risks involved [44]. The research concluded that co-curing large structures using Vacuum Assisted Resin Transfer Moulding (VARTM) "enabled reduced part counts (up to 80%), reduced fastener counts (up to 100%), and lower part fabrication costs as compared to conventional structures (30% to 50%)". The reduced number of parts was estimated to cut down

the assembly times by 50-80% resulting in further cost savings. An additional benefit of using of VARTM over traditional pre-impregnated carbon fibre cured in autoclaves, was the lower requirements on the material properties of the tooling, enabling the use of more inexpensive and easily processed materials.

1.2 Purpose

The primary purpose of the thesis is to evaluate and compare the four types of pi-joints illustrated in Figure 1.1. The 3D woven pi-joint consists of multiple layers of interlaced 0° and 90° fibres which are woven to a near-net-shape component. Similarly, the braided pi-joint is manufactured in a near-net shape, however, the braiding technique allows the fibre orientations to be tailored based on its specific applications. The L- and LU-style pi-joint were designed and manufactured for Automated Fibre Placement (AFP) machines using unidirectional dry fibres and then hot draped into the final shape. The evaluation of these pi-joints will be based on multiple factors including, strength, cost, and manufacturability. To achieve this, a method needs to be developed that allows the performance of the different factors to be weighed against each other.

The secondary purpose is to evaluate Non-Destructive Inspection (NDI) methods based on their ability to be scaled up for full-scale aircraft components as well as their effectiveness in detecting defects. The NDI methods that will be evaluated are X-ray, pulse-echo Ultrasonic Testing (UT), and active thermography.

Lastly, Finite Element (FE) models of the four pi-joint configurations should be developed that can predict the behaviour of the pi-joints including initiation of failure. Due to the complexity of these joints and limitations in the computational power available, modelling simplifications will need to be developed and evaluated.

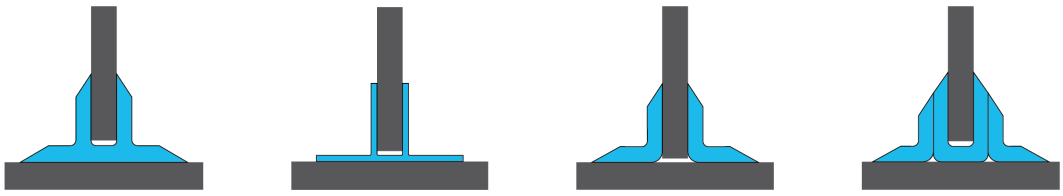

(a) 3D Woven **(b)** Braided **(c)** L-Style **(d)** LU-Style

Figure 1.1: Illustration of the 4 configurations of pi-joints evaluated.

1.3 Research questions

How do the four specified types of pi-joints compare to each other based on their strength, cost, and manufacturability?

How do the specified inspection methods compare to each other based on their ability to detect defects in pi-joints and scalability for use on entire aircraft wings?

How can the different types of pi-joints be modelled using Finite Element Analysis (FEA), and how well do these models predict the behaviour and failure?

1.4 Limitations

To manage the project with the given resources, the following limitations have been made.

- There are many designs of pi-joints, however this project will only evaluate the types of pi-joints presented in Subsection 1.3 made of carbon fibre and epoxy-based composite. Certification of aircraft structures requires extensive testing, such as fatigue testing and cyclic testing, together with variations in temperature and moisture. However, this project will be limited to static loading of the two main load cases; pull-off, and shear, as illustrated in Figure 1.2. These tests will be conducted at three temperature levels: colder, elevated, and room-temperature conditions, without controlling the moisture levels, see Subsection 5.3.

- The NDI will be limited to X-ray Computational Thermography (CT) scan, pulse-echo UT, and active thermography.

- No material characterisation will be performed, and all simulations will be based on preliminary material data from the manufacturer.

Due to delays during the project, the physical testing was postponed beyond the timeframe of this thesis. It was therefore decided that the physical testing should be a separate continuation of project for Heart Aerospace.

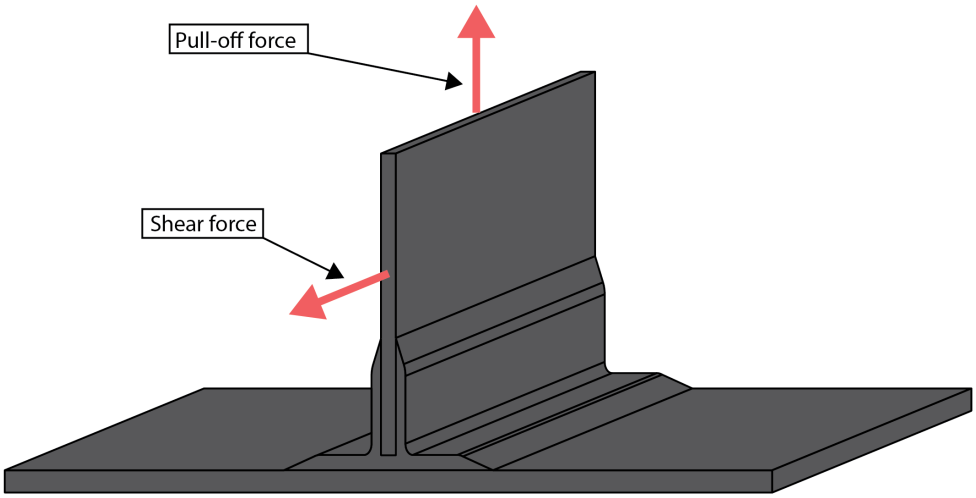

Figure 1.2: Illustration of the 4 configurations of pi-joints evaluated.

1.5 Unit systems

As this paper is a joint project of US and European entities, both the metric and imperial unit systems were used. All values are stated in both systems with the defining unit first, and the approximate conversion within parentheses.
The reason the defining unit varies is mainly due to the material properties being defined in the metric system whereas all geometrical dimensions relating to test fixtures and specimens are designed in the imperial system.

2

Theory

This section provides insights into the theory required to understand design, manufacturing and modelling decisions. It explains how 3D woven and braided composites works, and why these materials are particularly suitable for structural applications. Various manufacturing techniques are presented and described to better understand processes and design choices. Additionally, NDI methods are presented, describing their respective advantages and limitations.

2.1 3D woven composites

Unlike conventional 2D weaving resulting in a single ply of fibres in the two in-plane directions (X and Y), 3D weaving allows for multiple layers of fibres to be interlaced. This improves the mechanical properties such as increased out-of-plane strength as well as improved damage resistance [28]. The improved damage resistance is achieved by the out-of-plane fibres stopping crack growth and better distributes the load between plies [14] [47]. There are multiple classifications for 3D weaving techniques based on both fibre structure and manufacturing method. Common classifications are through-thickness and layer-to-layer (multi-ply) structures distinguished by the depth the out-of-plane fibres through the thickness of the laminate [50].

In the layer-to-layer 3D weaving process, fibres from any layer are interlaced with the neighbouring plies as illustrated in Figure 2.1b. These is commonly manufactured using orthogonal interlocking, meaning that the weft and warp tows are orthogonal to each other, at 0° and 90° [38].

There are 3D weaving techniques such as multi-axial 3D weaving that can incorporate fibre orientations of ±45° through more complex weaving techniques [50]. However, as of this writing there are no manufacturers producing pi-joints preforms with fibre orientations of ±45° at large scale and therefore these were not explored further in this project.

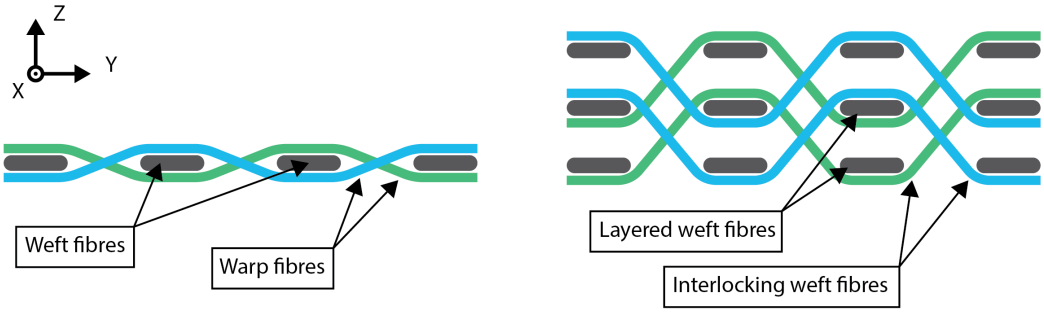

(a) 2D weaving **(b)** 3D weaving

Figure 2.1: Illustration of 2D and 3D woven fibres.

2.2 Braided composites

Similarly to the 3D weaving techniques, braiding can produce 3-dimensional near-net-shape preforms where the interlaced fibres provide improved load distribution. There are multiple techniques for braiding composites, some can produce preforms consisting of multiple interlaced plies such I-beams by using a grid of yarn-carriers that can automatically move in both the horizontal and vertical directions to create complex braiding patterns [43]. Other braiding techniques use a circular braiding machine to create tubular sleeves with continuous fibres around the circumference, however, these are limited to braiding a single ply of fibres in each sleeve [37]. These sleeves are then either laid up manually or over-braided directly onto a tool layer by layer to build thickness [29] [39]. This thesis focus on the latter approach used by A&P technology to braid pi-joint preforms.

A key feature of the braiding process is the flexibility in fibre orientations; by adjusting the feed rate of the braiding or the diameter of the tool, the fibre orientations can be adjusted within a continuous ply. Braided preforms can be both bi-axial and tri-axial allowing quasi-isotropic properties within a single braided ply thereby reducing the risk for interlaminar failures [37] [39].

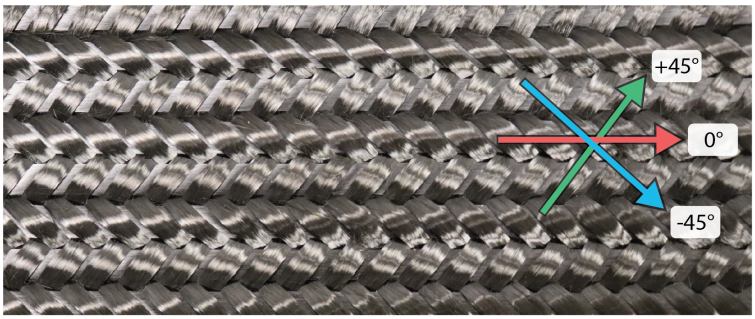

Figure 2.2: Illustration of triaxial braiding pattern.

2.3 Finite Elements Analysis

FEA is a computational tool for modelling structural behaviours. Assuming a foundational understanding of FEA, this section outlines the theory specific to the types of models built in this project. Mainly focusing on continuum shell elements and cohesive zone modelling, which combined enable modelling of thin-walled composites with potential interlaminar failures.

2.3.1 Continuum shell elements

In the aerospace industry, shell elements are commonly used for modelling sections such as wing skins, spars, and smaller sections of fuselages. However, solid elements are more suitable when the laminate is experiencing three-dimensional stresses or when the laminate thickness is large enough that shell theory is no longer accurate [26] [49].

Instead of using traditional shell or solid elements, a composite ply can instead be modelled using continuum shell elements. Such ply consist of a continuous layer of solid elements with an associated material coordinate system defining the directions for the orthotropic material properties. Similar to shell elements, continuum shell elements are suitable for structures where the in-plane dimensions, such as length and width, are significantly larger than the thickness. The continuum shell elements use three translational degrees of freedom per node as opposed to shell elements using translational and rotational degrees of freedom, see Figure 2.3. However, the continuum shell elements and the traditional shell elements have close correspondence in the kinematic behaviour [48]. The benefit over using traditional solid elements is that stresses and failure modes can be evaluated for each ply separately, and the interface between each ply can be modelled using cohesive zones.

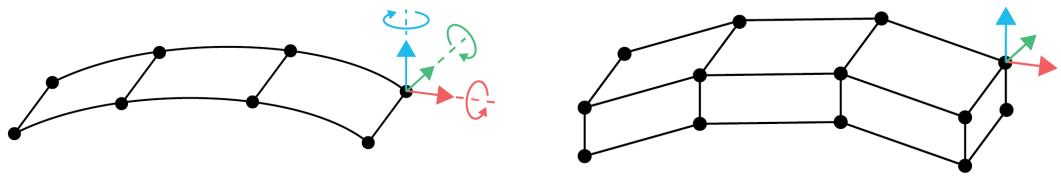

(a) Traditional shell elements **(b)** Continuum shell elements

Figure 2.3: Illustration of shell and continuum shell elements.

2.3.2 Cohesive zone modelling

There are multiple numerical methods for modelling crack initiation and propagation, such as delaminations in composites. Two common methods are Cohesive

Zone Modelling (CZM) and Virtual Crack Closure Technique (VCCT) [11]. As this project aimed to study where cohesive failures are likely to initiate, the crack modelling was done using CZM due to its ability to predict crack initiations anywhere within a cohesive zone, whereas VCCT requires a predefined initial crack.

Cohesive zone models are based on the cohesive law, also referred to as traction-separation law. This law dictates the behaviour of the cohesive zone prior to damage as well as the softening due to damage. The traction-separation law can be modelled as bilinear (triangular), trapezoidal, or exponential depending on the behaviour being replicated [42]. The simplest traction-separation curve is the bilinear one and its shape can be defined based on three parameters, the interface stiffness K (initial slope before damage), the interface strength τ_0 (stress at damage initiation), and the fracture toughness G_c (area under the curve), see Figure 2.4.

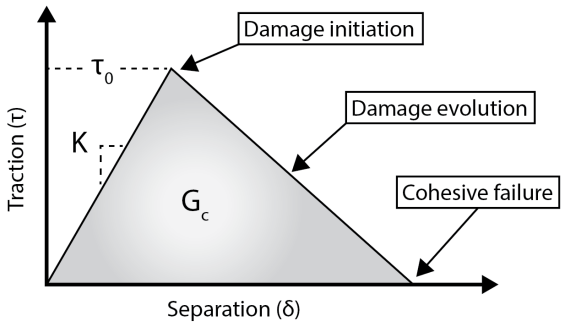

Figure 2.4: Illustration of traction-separation law.

There are three fracture modes considered in cohesive modelling, denoted Mode I-III as illustrated in Figure 2.5. Each of the fracture modes is defined by its own traction-separation law and therefore there are three fracture toughness's $G_{Ic}, G_{IIc}, G_{IIIc}$ as well as three interface strengths $\tau_{I0}, \tau_{II0}, \tau_{III0}$. Mode I represent peel opening and mode II and III are shear opening in the x-z and y-z planes. For an isotropic material such as the adhesive or resin, the shear fracture toughness and interlaminar shear strength is very similar in the two directions, and therefore the following simplification can be assumed $G_{IIIc} \equiv G_{IIc}$ and $\tau_{III0} \equiv \tau_{II0}$ [33]. Furthermore, as mode I represents the laminate being pulled (peeled) apart across the fibre direction, the failure stress τ_{I0} is often defined as the transverse tensile strength of the laminate. Similarly, the failure shear stress for mode II and III if often defined as the interlaminar shear strength of the laminate [3].

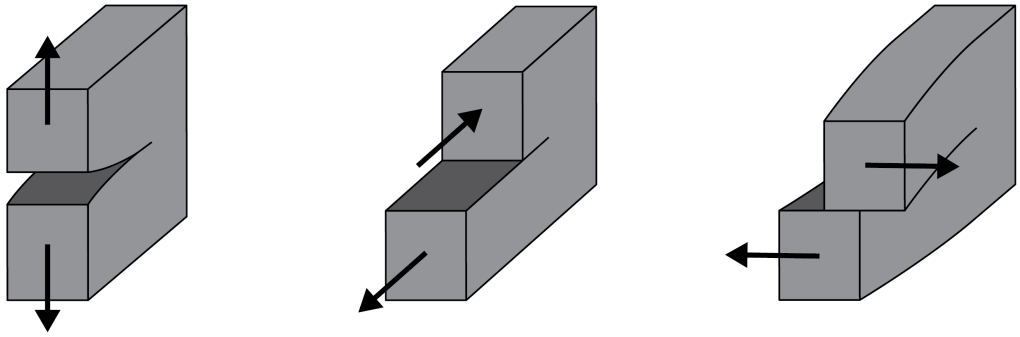

(a) Mode I (b) Mode II (c) Mode III

Figure 2.5: Illustration of the three fracture modes.

Cohesive zones can be modelled using either a surface-based or element-based formulation. The surface-based method uses a cohesive contact condition between a pair of surfaces, or between a surface and a set for nodes from the second surface [33]. This contact condition allows for surface separation but prevents penetration using the contact penalty method. The element-based method uses a single layer of cohesive elements between the surfaces that will potentially experience cohesive failures. These cohesive elements can be modelled as zero-thickness elements and the thickness used for the cohesive calculation is defined separately. The layer of cohesive elements is then connected to the mesh of the mating surfaces using either contact conditions such as FREEZE or TIE, or they can be connected through shared nodes if the nodes of the two mating surfaces as well as the cohesive elements are aligned, see Figure 2.6.

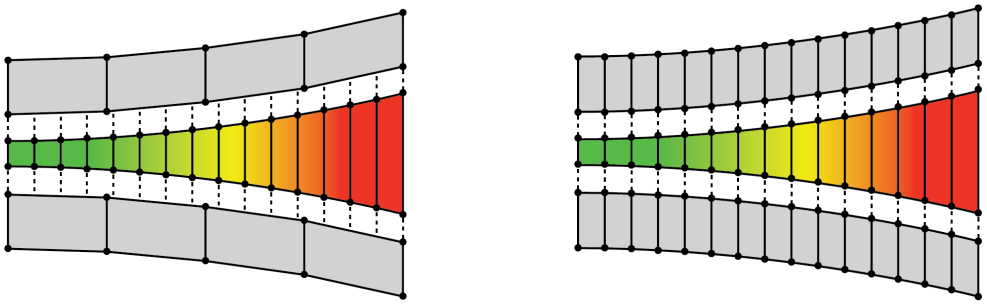

(a) Connected using contact entries (b) Connected through shared nodes

Figure 2.6: Connection methods for cohesive elements to base mesh.

To capture the behaviour of a cohesive failure a very fine mesh is required. A general guideline is to use at least three elements along the cohesive length in order to capture a stress distribution [4]. A too course mesh will overpredict the stiffness of the cohesive zone as each element will withstand a greater load before failure. If

the element would have been divided into multiple smaller elements the elements closest to the crack opening would have failed at a lower load and therefore resulted in a reduced overall stiffness earlier and more gradually. Cohesive models are also prone to experiencing computational instabilities caused by the rapid loss of stiffness when cohesive elements reach failure (debonding) [30]. To dampen these otherwise snapping displacements, a viscosity term can be introduced through Viscous Energy Dissipation (VED), which dissipates some energy during these rapid displacements and helps to computational solution converge. Too much energy dissipation will also result in an overestimation of the stiffness of the cohesive zone. To validate that these parameters do not overestimate the stiffness, a benchmarking study is commonly performed as presented in [41].

2.4 Tapered composites design principles

In the design of composite structures, tapering of the thickness is often required to optimize weight and structural performance. To achieve a tapered laminate individual plies need to be dropped at various locations along the structure, also called ply drops. Dropping one or multiple plies results in stress concentrations at the drop off location. To minimise the stress concentrations and the risk of failure, the number of plies dropped in one location should be kept to a minimum [1].

Other design principles for tapering composite structures are to always maintain one continuous ply above and below the plies which are being dropped. Furthermore, to reduce the out-of-plane failure modes, the staggering distance should be at least 20 times larger than the thickness of the dropped plies in the primary load direction and at least 10 times in the secondary load directions [12], see Figure 2.7.

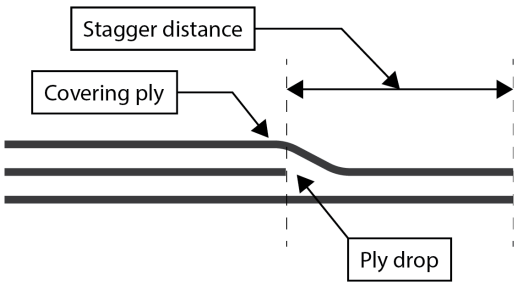

Figure 2.7: Illustration covering ply, staggering distance and ply drop.

2.5 Composites manufacturing techniques

There are many different manufacturing techniques for composites, this section summarizes the essential theory of the used manufacturing techniques such as AFP, hot

draping and VARTM. The theory presented in each subsection is essential for understanding how the manufacturing process impacts the design of composite pi-joints.

2.5.1 Automated Fibre Placement

AFP is one of many methods used to scale composites manufacturing and replace the manual labour of hand-layup. The process uses robotic arms to lay up composite materials for parts such as wing skins, spars and fuselages [12].

A heating system, such as an infrared laser, is used to heat the resin in the tows of pre-impregnated (prepreg) fibres, or for dry fibres heating the thermoplastic veil, to make it tacky enough to stick to the tooling surface or underlaying plies. A compaction roller is then used to compact the tows [16].

AFP systems can lay both prepreg and dry fibre tows. Depending on the AFP system, the number of tows laid down simultaneously vary from a single spool up to 32 spools. The width of the individual tows ranges from 1/8" (3.2 mm) to 1/2" (12.7 mm). All spools can typically be individually controlled, which allows for lay up on complex geometries [19] [25].

Although AFP reduces the risk of human error, it has other manufacturing difficulties. Defects such as overlaps, gaps, wrinkles and missing tows can still occur.

2.5.2 Hot draping

Hot draping is a method for preforming 3-dimensional geometries of prepreg or dry-fibre laminates instead of laying up the fibres directly onto a curved tool. This method is commonly used for shaping bends such as sub laminates of an I-stringer [40].

Hot draping works by heating up the uncured laminate such that the thermoplastic veil of dry-fibres, or the resin in prepreg fibres, softens and allows the fibres to slide against each other. This is done in combination with vacuum pressure or even external pressure using an autoclave to conform the preform against a tool. By letting the preform cool down before removing the vacuum pressure, the preform will maintain the deformed shape.

Bending a preformed laminate requires plies to slide along each other as the radius of a curve will increase for each ply moving away from the tooling surface. As the thermoplastic veil or resin is sticky, they will resist this sliding, and the created tension between plies may lead to various defects and spring-back. Plies with fibres oriented along the axis of bending will experience this tension in the transverse direction which have very low strength prior to curing. As illustrated in Figure 2.8 this can result in gaps where fibres are being pulled apart unless supported by outer

plies. As the outer plies experience tensions, the plies close to the tooling surface will be compressed. This in-plane compression may lead to wrinkling of fibres which in turn cause out-of-plane defects [13].

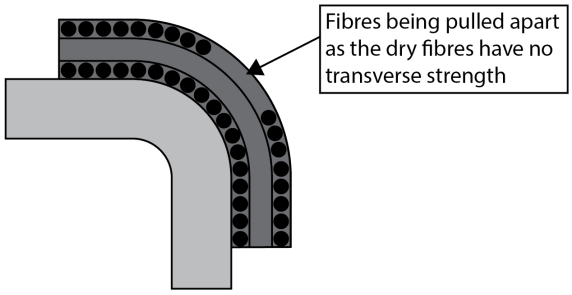

Figure 2.8: Illustration of defects from hot draping.

2.5.3 Vacuum Assisted Resin Transfer Moulding

The VARTM process uses a difference in pressure to infuse resin into the dry fibres. The vacuum also improves the compaction of the fibres, minimizing the air trapped between plies, thereby also achieving a high fibre volume fraction. When designing an infusion setup, it is important to consider where to position the resin inlet port(s), vacuum port(s), as well as potential flow media, and thermocouples. The position of resin inlet ports and flow media tailor how well the resin flows through different regions of the laminate, and if done correctly the laminate should be fully saturated before reaching the vacuum port(s) [31]. Flow media is a consumable layer used to achieve high flowrates of resin during infusions. It allows resin to reach all regions of a component by minimizing the distance the resin must flow through the fibres which is significantly slower.

Trapping air inside the laminate results in voids and dry spots, causing stress concentrations and reduced mechanical properties. To avoid introducing additional air bubbles, the resin is commonly de-gassed under vacuum prior to infusion [7].

One important property for resin infusion is the permeability of the laminate, meaning how well it lets resin flow through. This property is affected by multiple factors such as the orientations of the plies and the compaction during layup. For example, UD fibres have significantly lower permeability in the transverse direction where the resin must flow across the fibres as opposed to the longitudinal direction where natural opening between the fibres are formed [15]. Woven materials also facilitate higher flow as the interlaced structure of the tows leaves openings for the resin to flow [32].

2.6 Non-destructive inspection methods

There is a multitude of NDI techniques used today for assessing the quality of composites structures; both for detection of manufacturing defects as well as evaluation of damage or material degradation. This chapter aim to introduce and summarize the key features of the non-destructive inspection methods used in the project.

2.6.1 X-ray computed tomography

X-ray computed tomography (CT) scanners used for inspection of composites works similar to the CT scanners use by the medical industry; with the exception that the object being inspected is rotated as opposed to the source and detector [2]. X-ray scanning works by emitting X-rays that pass through the specimen and measuring the energy of the received rays on the other side [8]. This can be done either using a cone beam against a plate detector or as a fan beam against a line detector. Depending on the material characteristics, such as density, and the thickness of the object, various amounts of the X-rays will be absorbed or scattered. The plate or line detector then create a 2D or 1D grayscale image, and after scanning the entire object from all directions, the grayscale images can be used to construct a 3D representation of the object. The 3D models can then be sliced to display cross-sectional images of the object from any direction. Since the different materials within a laminate such as fibres and resin have different material properties they will absorb/scatter different amounts of the X-ray. The CT-scan can therefore not only identify defects such as void and porosity but also visualize fibres and plies within a laminate [10].

The resolution of a scan is dependent on the focus of the X-ray beam, meaning the size of the area being inspected per data point. An increase in resolution therefore requires significantly more time and energy hence larger cost. CT systems used for quality control of composites commonly use a voxel resolution between 80–160 μm, however for studying individual fibres a much finer resolution is required [2].

2.6.2 Ultrasonic inspection

Ultrasonic inspection is a group of inspection methods based on emitting an ultrasonic sound wave and analysing the response; two common techniques are TT and Pulse-echo [21]. Both these techniques utilise a transducer coupled to the inspection surface using a liquid couplant (usually water). However, the difference between the techniques is how the signal is received. TT uses a separate receiver on the backside of the surface being inspected whereas the Pulse-echo method waits for the signal to reflect off the backside and return to the transducer.

The signal measured by the receiver is then interpreted based on the remaining energy of the ultrasonic wave [20]. A solid laminate with low porosity and no defects

will yield a strong signal with low losses compared to a signal passing through porous laminates where much of the energy will be scattered. A void or delamination within a laminate substantially reduce the energy of the ultrasonic wave that reaches the receiver in the case of through-transmission, meaning the inspection detects the defect but cannot specify at what depth the defect occurs. Similar to how sound waves are reflected by the back surface, much of the sound wave is reflected off voids which, if received by a pulse-echo system, would appear as a returned signal at a shallower depth than the backside, indicating a defect.

The results from ultrasonic inspections are commonly presented as A-scans or C-scans. An A-scan displays the measurement in a single point as a graph where the horizontal axis represents the time it took for the signal to return (depth into laminate), and the vertical axis represents the strength of the measured signal [27]. Since A-scans only test a single point at a time it does not provide an overview of where defects or delamination occur in a part. Therefore, operators sweep transducers systematically along the inspection surface, marking locations on the laminate where abnormalities are observed.

By automating the sweeping of the transducer along the surface using a gantry or robotic arm which position can be tracked, a C-scan can be created as an image where the colour and brightness of each pixel represents the data in each measured point [27]. This data can then be displayed as images presenting information such as the strength of the measured signal indicating the presence of defects, or the depth of the strongest reflected signal indicating how deep into the laminate the defects are present.

2.6.3 Pulsed thermography

Thermography is a group of multiple inspection methods all based on the thermodynamic properties of the part being inspected; and are typically divided into two different categories, passive and active [18]. The passive technique uses an infrared (IR) camera to visualize temperature differences caused by self-heating, which can result from fatigue damage, among other factors. The active techniques such as pulsed thermography (PT) are based on external excitation to generate heat in the component and IR cameras are used to observe the dissipation of heat over time. The presence of defects such as voids or delaminations will alter the behaviour of the diffusion and appear as variations on the IR camera [5].

Nsengiyumva et al. summarized in [17] that previous studies indicate active thermography can only detect defects within a depth of 4 to 5 mm (0.16–0.2") in carbon composite laminates.

3

Pi-joint design

This section details the design of the pi-joints, the load cases along with the design considerations for the test fixtures, as well as the FE modelling method used. Since many design choices are dependent on the selected manufacturing methods, it is important to have an overview of this process. Therefore, this section will begin with a summary of the overall manufacturing process the specimens were designed for.

Firstly, the webs are resin infused and cured as flat plates which are then trimmed to size. The webs are then wrapped in release coated material so that they can be used as tooling during the infusion of the pi-joints and skins, note that these two are co-cured as a single component. After curing, the webs are extracted and the release materials removed. Lastly, the webs are bonded back into the pi-joints to form a secondary bond between the pi-joint clevis and the web. Figure 3.1 illustrates these main manufacturing steps. Each pi-joint configuration has slight variations to the individual steps due to their specific requirements and is further detailed in Section 4.

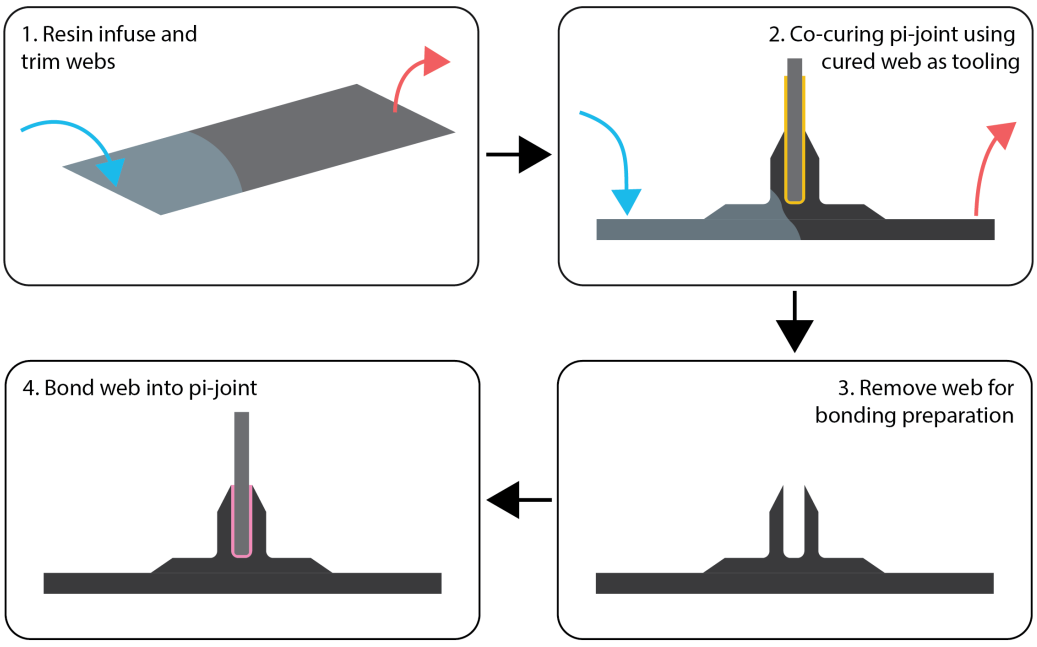

Figure 3.1: Illustration of key steps in the manufacturing process.

3.1 Lamina properties

To reduce the number of unknown material parameters and potential failure points due to material mismatch, all webs, skins, and AFP preformed pi-joints were manufactured using Hexcel HiTape fibres with Hexcel HiFlow 1078-1 epoxy [24]. As of this writing there is no public datasheet for the Hexcel HiTape fibres.

Preliminary proprietary material data from the manufacturer provided the longitudinal and transverse stiffness, as well as the tensile, compressive, and shear strengths. The remaining parameters, such as shear moduli and Poisson's ratios were initially defined based on values from similar materials such as Hexcel IM7 8552 and Toray T650 + Solvay (Cytec) 5320-1 [23] [45]. Another unknown parameter was the volume fraction of fibres in the tested laminates. To assure that the volume fraction of this projects' test specimens matches the volume fraction of the tested laminates as best as possible, the infusions were performed according to the processing recommendations for the HiFlow 1078-1 resin [24].

Furthermore, the preliminary test data also provided the stiffnesses and ultimate strengths of three balanced and symmetric layups with various distributions of $0°$, $90°$, and $\pm 45°$ plies. Using the initial set of material parameters and classical laminate theory through the software ESAComp, the stiffnesses of provided laminates were estimated and the results compared to the test data. The unknown material properties were then adjusted iteratively to better match the coupon test results. The final material properties resulted in laminate properties within 5% of the preliminary tests for a quasi-isotropic layup.

3.2 Pi-joint selection and design

To maintain consistent terminology the following naming convention was introduced. Figure 3.2a illustrates the terms used to describe the general pi-joint while Figure 3.2b shows specific terms used for L- and LU-style pi-joints.

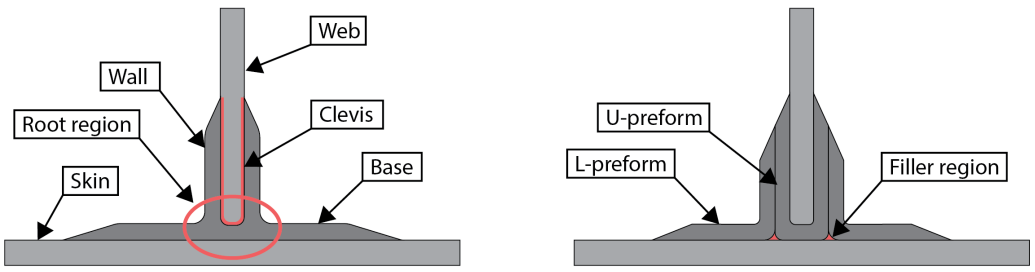

(a) General pi-joints terms **(b)** L- and LU-Style pi-joint terms

Figure 3.2: Illustration of pi-joint naming convention.

3.2.1 Selection of commercial pi-joints

The two commercial pi-joints selected are based on two different methods of achieving a near-net-shape pi-joint preform, one using 3D weaving and one using continuous braiding.

The 3D woven pi-joint used in this project is manufactured by Bally Ribbon Mills (BRM) and is woven from Hexcel HexTow IM7 fibres. The weaving method produces a pi-joint preform consisting of 8 layers of interlaced fibres in the base and 4 layers in the clevis walls, Figure 3.3 shows the dimensions of the pi-joint. All fibres run either along or across the preform, meaning only in the 0° - or 90° -directions.

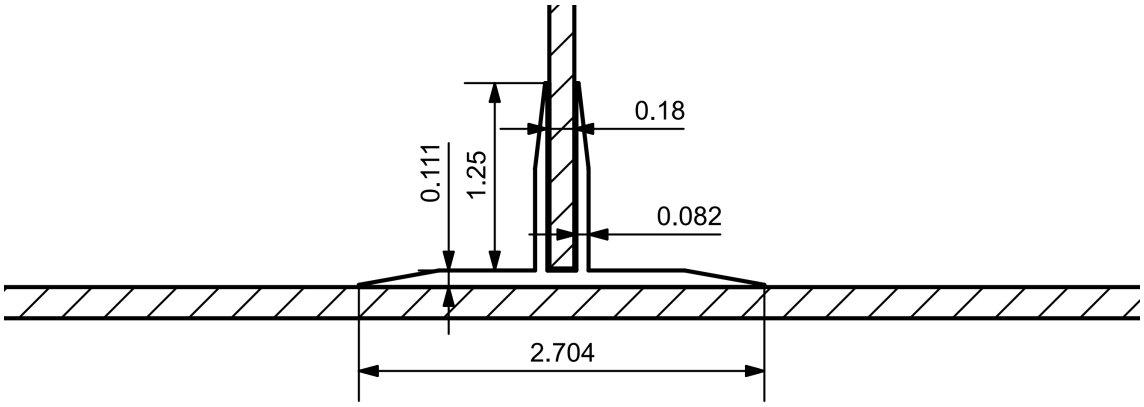

Figure 3.3: Drawing of 3D woven pi-preform from BRM (units in inches).

As mentioned in Subsection 2.2 the braided pi-joints consist of a single layer of braided fibres. The braided pi-joints from A&P technologies with comparable dimensions to the 3D woven pi-joint from BRM have significantly thinner walls and base. Therefore, a larger braided pi-joint preform with higher fabric weight was selected to achieve a more comparable strength to the 3D woven pi-joint. The size of the braided pi-joint was selected based on availability and limitations in the test fixture; the base of the pi-joint could not exceed 7.5" (190.5 mm). The largest braided pi-joint that fits these requirements had a fabric weight of 1516 gsm, and a base thickness of 0.067" which is still 40% thinner than the base of the 3D woven preform. To accommodate the larger braided pi-joint, the size of the skins was increased along with the thickness of the webs. These modifications are described in more detail in Subsection 3.5.

Note, the choice of suppliers for this project was based on availability and is not intended as a recommendation of any specific manufacturer.

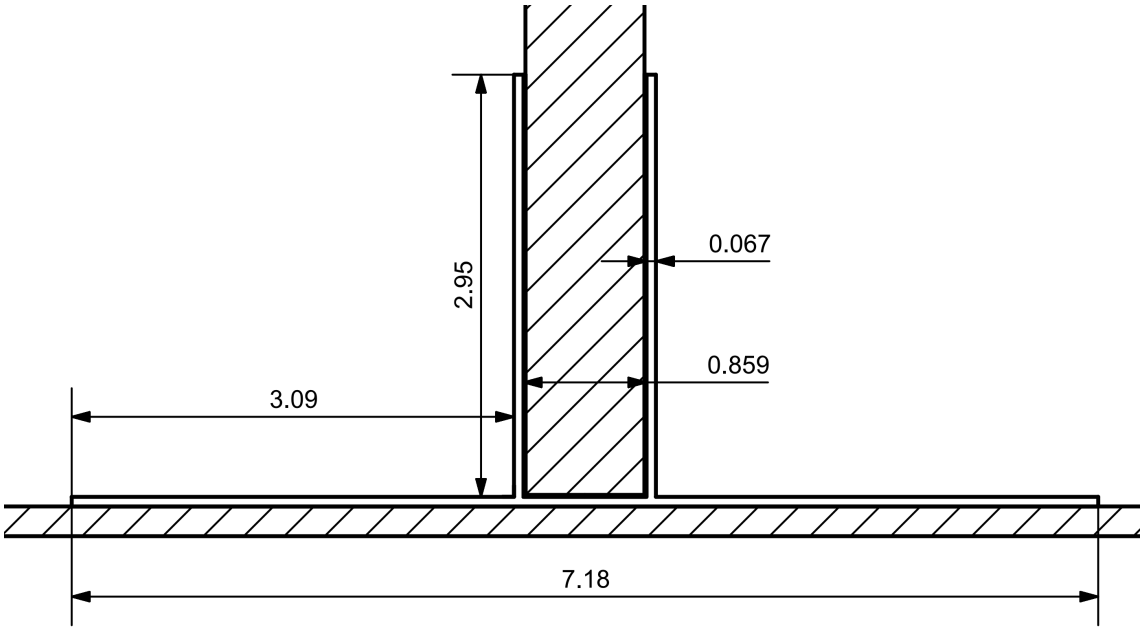

Figure 3.4: Drawing of Braided pi-preform from A&P Technology (units in inches).

3.2.2 General targets and requirements for AFP preformed pi-joints

AFP preformed pi-joints refers to the L- and LU-style pi-joints using laminate preforms laid up by AFP machines. The sizing and layups for the pi-joints used in this project were designed based on common composite design principles presented in Subsection 2.4 and manufacturing limitations. The designs could be further optimized by use of FEA.

The use of ±45° fibres improves the shear strength of the joint, and the 0° fibres along the pi-joint improve the bending stiffness of the web attached to the pi-joint, acting as flanges of a T-beam. To achieve high a strength in both load cases, the AFP preformed pi-joints were designed with a (50/50/0) target distribution, meaning 50% of the fibres in the 0-direction, 50% in the ±45-directions, and no fibres in the 90-direction.

The L-preforms were designed to have comparable dimensions to the 3D woven pi-joint as well as being balanced and symmetric. This was achieved using an 8-ply layup with a total thickness of 0.083” (2.11 mm), 1.2% thicker than the walls of the 3D woven pi-joint. Since the tolerance of the final bondline thickness between the pi-joint and the web is critical, it is especially important that the pi-joint walls are symmetric to minimise any warping of the clevis caused by unsymmetric thermal expansion.

To match the 3D woven preform size, the unfolded width of the L-preforms should be 3” (76.2 mm), see Figure 3.5. However, as the minimum recommended tow length

for AFP was 4.5” (114.3 mm) to avoid potential problems due to fibres not sticking, the preforms needed to be widened. This meant that any layer of ±45° fibres need to be at least 3.18” (80.8 mm) wide to have a 4.5” (114.3 mm) diagonal. Additionally, as the 0° fibres are laid down along the length of the pi-joint and each tow has a fixed width of 0.25” (6.35 mm), meaning any 0° layer must have a width evenly divisible by the tow width, see Figure 3.5

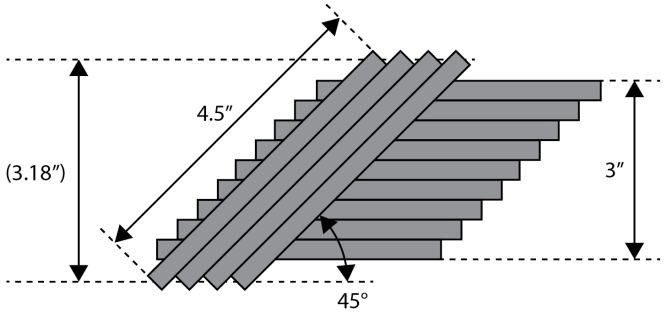

Figure 3.5: Illustration of width limitation on L-preforms.

Lastly, the inner radius of the bend was designed to be 0.25” (6.35 mm) for the hot draping process based on availability of tooling. This gives an estimated outer radius of 0.32” (8.13 mm).

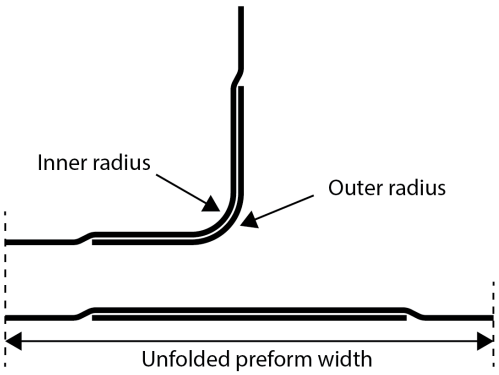

Figure 3.6: Illustration of unfolded preform width.

To minimise stress concentrations in the transition from web to pi-joint as well as from pi-joint to skin, the thickness of the joint was gradually decreased by dropping plies. The ideal stagger ratio of 1:20 for primary structures would result in a pi-joint significantly larger than the 3D woven pi-joint. Therefore, the stagger ratio requirement was reduced to 1:10 commonly used for secondary structures as discussed in Subsection 2.4.

After the L/U-preforms have been laid up they were formed into the L/U-shapes by hot-draping. As mentioned in Subsection 2.5.2, fibres in the outermost plies should

not be oriented along the axis around which the preform is bent as it can result in fibres pulling apart leaving gaps. Therefore, the outermost plies for both L-preforms and U-preforms were limited to orientations of ±45° .

3.2.3 L-style pi-joint

Based on the manufacturing limitations and design targets the final layup for the L-preforms in the L-style pi-joints was [+45/0/-45/0/0/-45/0/+45]. Dropping the two centremost plies first keeps the layup symmetric up until the second ply drop and balanced until the third ply drop, see Figure 3.7. Additionally, it allowed the width of the preform to be minimised as the limiting factor was the diagonal length of the ±45° plies. The two outermost +45° plies acts as covering plies whilst also keeping the laminate from pulling apart during the hot-draping process.

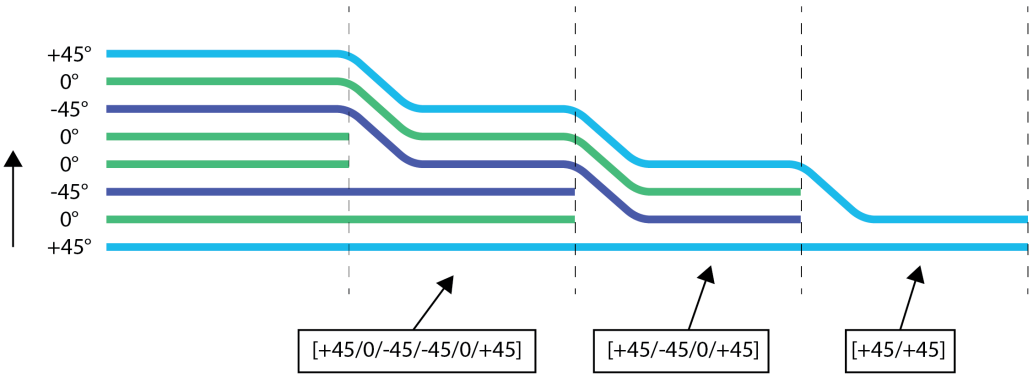

Figure 3.7: Illustration of ply drops by edges of L-preform.

When dropping 2 plies together the required stagger ratio of 1:10 meant a minimum stagger distance of 0.208” (5.28 mm) on either side of the laminate. Increasing the ply widths by 0.25" (6.35 mm) on either side at each ply-drop location meant that all ply widths are evenly divisible by the tow width and the resulting stagger ratio is 1:12. The total width of the unfolded L-preform is therefore 4.5” (114.3 mm).

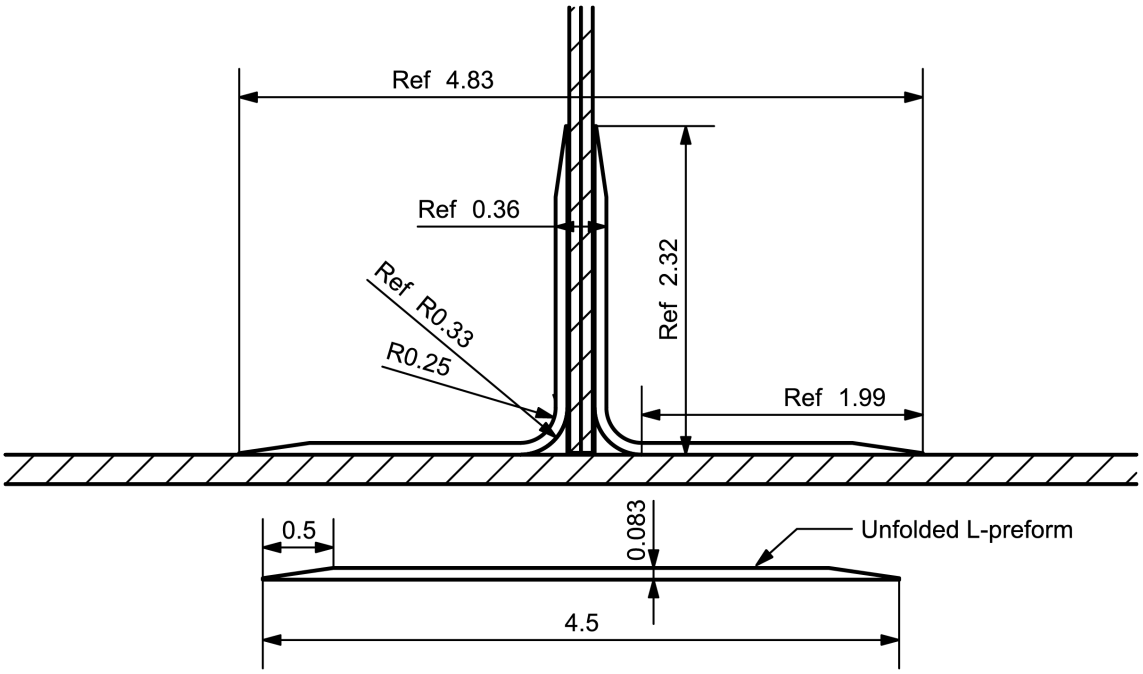

Figure 3.8: Drawing of the L-style pi-joint.

3.2.4 LU-style pi-joint

The LU-style pi-joint was designed as a reinforced version of the L-style pi-joint with 4 additional ±45° plies . The LU-style pi-joint consists of two sub-laminates (L-preform and U-preform) co-cured to form the clevis walls as illustrated in Figure 3.9.

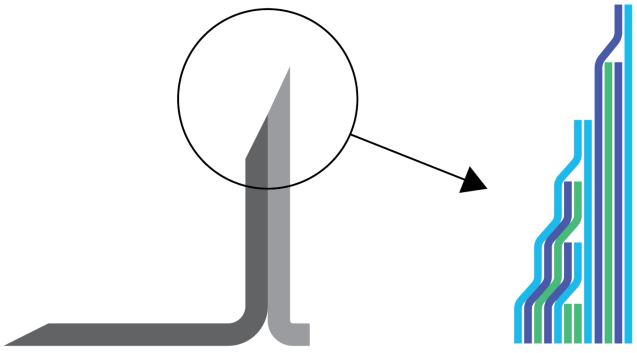

Figure 3.9: Illustration of the overlap of the L- and U-preforms.

To avoid warpage of the clevis walls, the combined layup of the L- and U-preform was designed to be symmetric. To minimise distortions and defects caused by hot-draping the U-preforms 180° the thickness was limited to 4 plies as opposed to the 8 plies of the L-preform. The different number of plies in the two sub-laminates

meant that each sub-laminate had to consist of an asymmetric layup for the combined laminate to be symmetric. The final L-preform layup for the LU-style pi-joint was [+45/0/0/+45/-45/0/-45/+45] and the U-preform layup was [+45/-45/0/-45].

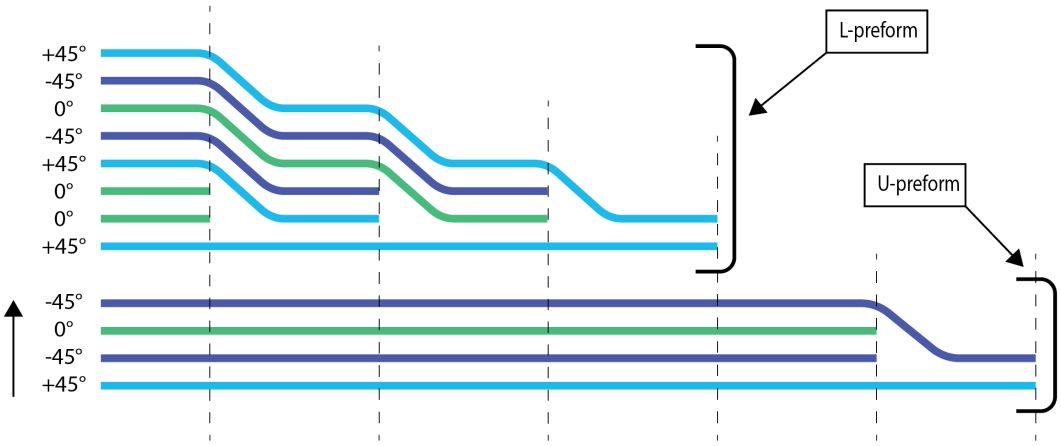

Figure 3.10: Illustration of ply drops by edges of LU-preform.

It is important note that the local Material Coordinate System (MCS) of the U-preform rotates 180° around the x-axis as the U-preform is draped around the web. In other words, on one side of the web the local y-axis points upwards and on the other side it points downwards, see Figure 3.11. The continuous +45° fibres would therefore appear as -45° fibres if viewed from the back side of the web and vice versa. To maintain symmetric layups for the combined laminates on both sides of the web, the L-preforms on either side of the web must not be mirrored versions of each other but rather two identical layups rotated such that the L-preforms MCS match the U-preforms MCS on both sides, see dashed circle in Figure 3.11.

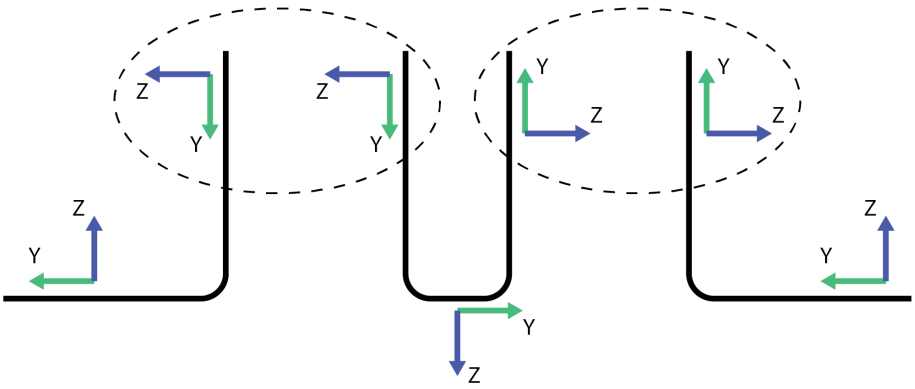

Figure 3.11: Illustration of material coordinate systems for LU-preforms.

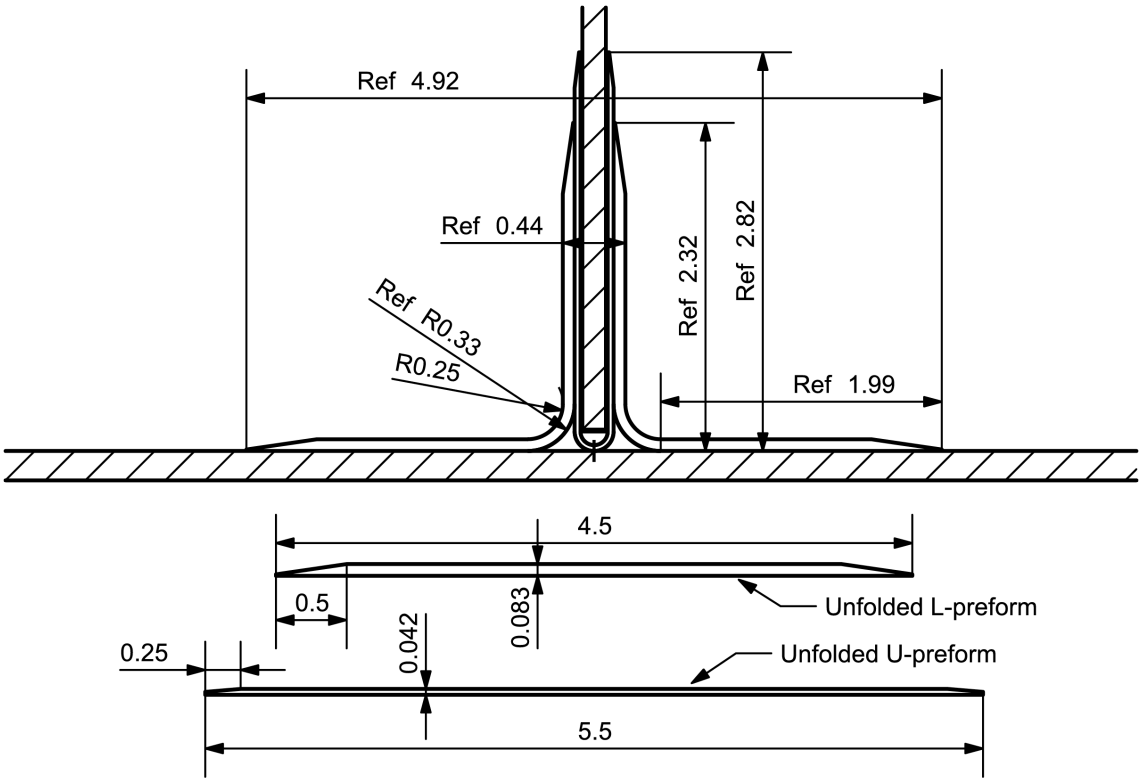

Figure 3.12: Drawing of the LU-style pi-joint.

3.3 Skin layup

As the aim was to investigate the relative strengths of the pi-joint configurations regardless of the characteristics of the skin, the layup was designed to be symmetric, balanced, and near quasi-isotropic. Based on a 0.2" (5 mm) target thickness of the skin defined in accordance with Heart Aerospace's preferences, and a cured ply thickness of 0.0104" (0.264 mm), a 20-ply layup was chosen.

Using four quasi-isotropic groups of [90/-45/+45/0], along with four additional plies added in the middle of the laminate to maximize the isotropic behaviour. The final layup for the skin was [90/-45/+45/0/90/-45/+45/0/90/0]s.

3.4 Web layup

The web laminate was designed to be 0.154" (3.91 mm) to match the 0.18" (4.57 mm) clevis width of the 3D woven pi-joint, including a bondline on either side of the web. The bondline thickness was designed to be 0.013" (0.33 mm) per manufacturer recommendation in the FM300-2 product datasheet [46].

To achieve the target laminate thickness, a balanced and symmetric quasi-isotropic layup of 16 plies was used with the following stacking sequence [90/-45/+45/0]2s.

3.5 Sandwich web

As mentioned in Subsection 3.2.1, the braided pi-joints required a thicker web compared to the solid laminate webs used for the 3D woven and AFP preformed pi-joints. Since the clevis gap of the braided pi-joint is 0.864" (21.9 mm), this pi-joint is more suited for a web made as a sandwich panel.

During the pull-off and shear tests, the webs are clamped by the test fixtures which means that the sandwich panel need to withstand a significant clamping force and allow bolt holes to be drilled through it. The design of the sandwich webs used a honeycomb core bonded to the cured web laminates using a film adhesive and reinforced in the clamping regions with a potting compound. This decision was based on material availability and lead times.

The defining compressive load case for the web was the pull-off test, since the tensile machine uses a wedge action grip where all force is transferred using the friction between the grip and the specimen. To strengthen the sandwich web, the clamping area needed to be reinforced with a high compressive strength potting compound to withstand the clamping force applied by the grip.

Additionally, since the sandwich webs are used as tooling during the co-curing of the pi-joints it is also important that both the adhesive used to bond the sandwich core as well as the potting compound have a glass transition temperature higher than the 350°F(177°C) required for the infusion.

Based on these requirements, the following materials were selected.

Table 3.1: Materials used for sandwich webs.

Core material	Euro-Composite ECA-R 4.8-64
Film adhesive	Syensco FM309-1M
Potting compound	Loctite EA 9825

The core material Euro-Composite ECA-R 4.8-64 was chosen based on availability. Both the film adhesive FM309-1M and potting compound Loctite EA 9825 have glass transitioning temperatures above 350°F(177°C). Additionally, the potting compound has a compressive strength of 91.7 MPa (13.3 KSI).

3.6 Design requirements and test fixtures

This section presents two load cases, pull-off and shear, for which all the pi-joints will undergo physical testing. To ensure the tests replicate in-service conditions the design of the pull-of fixture must minimise the bending moments occurring near the tip of the pi-joint base. Additionally, for the shear fixture the force should be as close to coplanar to the co-cured interface as possible.

3.6.1 Pull-off load case

The pull-off load case is defined by a load acting on the web, pulling it vertically from the skin, given that the skin is horizontal. When used in aircraft structures, the skins are commonly reinforced using stiffener elements to minimise the local out-of-plane deflection of the skin. The pull-off specimens used in this project does not include any stiffener elements and hence will experience greater than normal deflection under the pull-off load case. This bending of the skin can result in unwanted peeling effects at the edges of the pi-joint base.

To minimise the bending moments near the edges of the pi-joints, the test fixture was designed to use a four-point support, see Figure 3.13. The spacing of the supports were calculated by using 1D beam theory minimizing the bending moment for each pi-joint configuration, for spacings see Table 3.2 and Figure 3.13.

Table 3.2: Support spacing for pull-off tests.

Pi-joint configuration	Upper support	Lower support
L-style	8" (203.2 mm)	11" (279.4 mm)
LU-style	8" (203.2 mm)	11" (279.4 mm)
3D woven	5" (127 mm)	10" (254 mm)
Braided	10" (254 mm)	12" (304.8 mm)

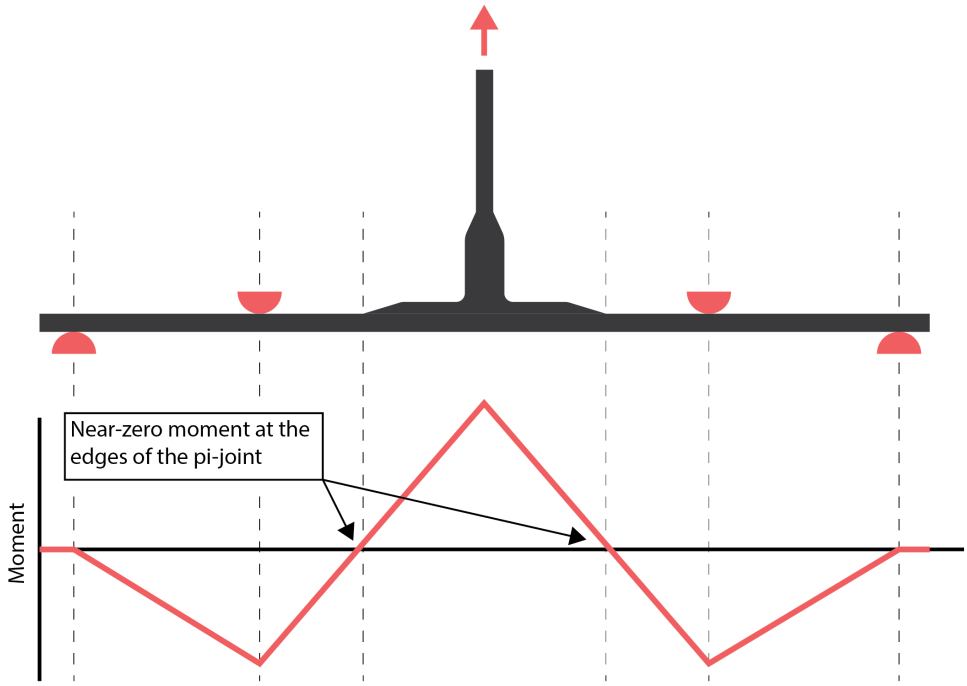

Figure 3.13: Illustration bending moment in skin during pull-off testing.

3.6.2 Shear load case

The shear load case is defined by a force acting horizontally on the web in-line with the pi-joint, given that the skin is horizontal. When a spar (beam) of an aircraft wing act as a beam in bending due to lift forces, the web of the spar will experience shear forces which the pi-joints need to transfer to the skins.

To test the shear load case isolated, the load application points of the fixture were designed to be coplanar with the co-cured interface between the skin and pi-joint. However, any compliance in the fixture will result in compressive stresses along one edge of the web and tensile stresses in the other edge, as illustrated in Figure 3.14. This is a result of the fixtures resisting the moment around the test specimen caused by the height difference between the bolt patterns in the web and the skin. To reduce the effect of these tensile and compressive forces in the web, the width of the shear specimen was increased to 6” (152.4 mm) as to increase the leverage of the resisting forces and therefore decreasing their magnitude.

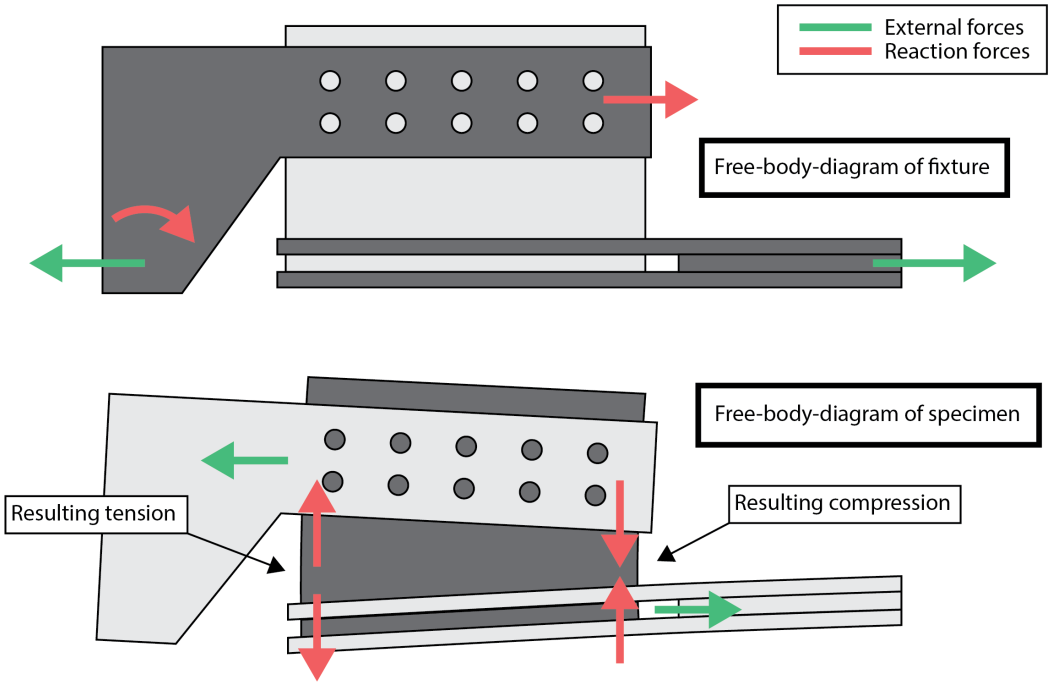

Figure 3.14: Free body diagram of shear test fixture and shear specimen with exaggerated deformation.

The test fixture was designed to be bolted to the skin and web, clamping the laminates, see Figure 3.15. The bolt pattern was dimensioned using equations provided in NASA's simplified design guides for bolted joints, and all frictional forces were neglected to eliminate dependence on the bolt torque [22].

The final bolt pattern in the web consisted of two rows of five 1/4" (6.35 mm) bolts, spaced 1" (25.4 mm) apart horizontally and 1.25" (31.75 mm) apart vertically. As the height of the pi-joint walls vary for the four pi-joint configurations the lower row of the bolt patterns was positioned 1" (25.4 mm) above the theoretical height of each pi-joint.

The bolt pattern in the skin had the same 1" (25.4 mm) spacing between the bolts but only one row per side of the pi-joint. The spacing between the two rows of bolts were 7" (177.8 mm) for the 3D woven, L-style, and LU-style pi-joints and 10" (254 mm) for the larger braided pi-joint.

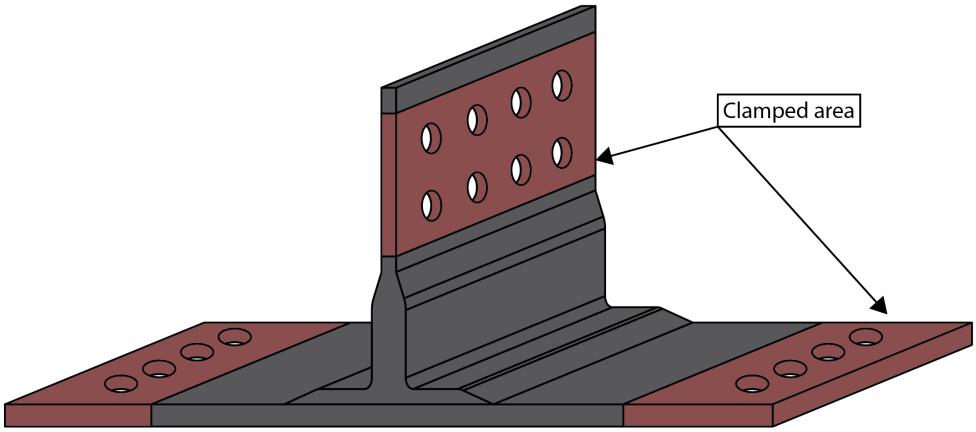

Figure 3.15: Illustration of clamped regions during shear testing.

3.7 Finite element modelling

FE models were developed to predict the response of the pi-joints in the load cases described in Subsection 3.6. This section describes the chosen material and failure models and methods used to reduce the model sizes such as symmetry conditions, homogenization of ply groups, and optimisation of cohesive zones. This section also describes the boundary conditions used to model the fixtures as well as a benchmarking study used to validate the behaviour of the cohesive elements.

The models were built using the FE pre- and post-processor HyperMesh from Altair and solved using the Altair Optistruct FE solver. The following table summarizes the element types, and solver cards used to model the various components of the pi-joints.

Table 3.3: Solver cards used for FEA models.

Component	Element type	Property card	Material card
Solid plies	CHEXA8	PCOMPLS	MAT9OR
Filler regions	CHEXA8/CPENTA	PSOLID	MAT1
Cohesive elements	CIFHEX8	PCOHE	MCOHED

All plies and homogenized ply groups were modelled using the MAT9OR material card in Optistruct, this material card is used for linear, temperature independent and orthotropic materials. The simulations for both load cases were performed using room temperature material properties without regards to initial stresses caused by temperature differences during the manufacturing process.

In analysing the composite failure, the Tsai-Wu failure theory was used through the material failure card MATF in Optistruct. However, the MATF card does not consider any stiffness penalty when an element has failed. Therefore, the ultimate failure loads will be overestimated.

3.7.1 Computational simplifications

Due to the large out-of-plane forces resulting from the pull-off load case, solid elements were used for both the skins, webs, pi-joint preforms, as well as the resin filler regions. The plies in the pi-joint preforms were modelled ply by ply with one layer of solid elements each. However, modelling the pi-joints as individual plies combined with cohesive elements to capture crack propagations, results in very computationally heavy models. To reduce the computational time, a few simplifications of the models were therefore made.

The first simplification was homogenizing the plies of the webs and skins as groups of 4 plies sharing a single element in thickness. The material properties of these elements were derived using Altair ESAComp as the laminate properties of an equivalent 4-ply layup.

Additionally, whereas the physical test specimens were 3" (76.2 mm) and 6" (152.4 mm) wide respectively, the width of the FEA models was reduced to 1" (25.4 mm). This trade-off allowed for better resolution at the cost of larger edge-effects.

To further reduce the size of the FE models the webs were shortened to end 5 mm (0.2") above the pi-joints and the whole models were halved by using symmetry through the midplane of the webs, see Figure 3.16. As discussed in Subsection 3.2.4, the L-preforms on either side of the webs are not mirrored copies of each other but rather rotated 180° . However, since the preforms are balanced with ±45° fibres, the effect of this should be minimal. Similarly, the +45° plies in the skin would be mirrored to -45° fibres through the symmetry plane, but since the skin laminate is balanced this was deemed an acceptable simplification.

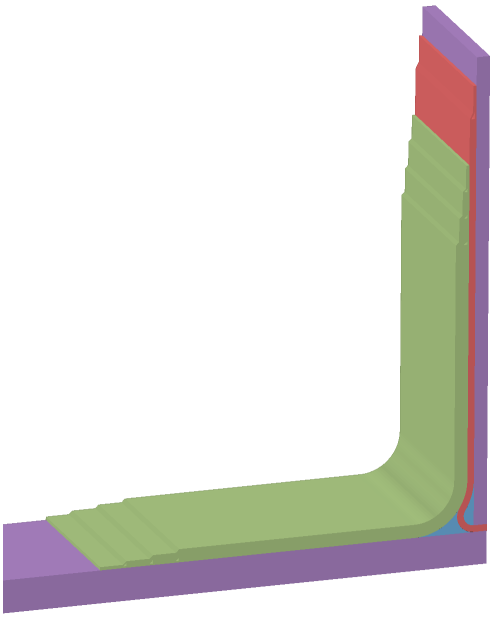

Figure 3.16: FE model with web shortened to end 5 mm above the pi-joint.

3.7.2 Boundary conditions and fixtures

All nodes along the symmetry plane were constrained to only move within the symmetry-plane and rotate around the symmetry-plane normal. Due to the geometrical nonlinearity of the specimen the models will experience stress stiffening, meaning that the geometry will get stiffer with increased displacement. This, combined with the use of cohesive elements whose stiffness will be reduced upon failure, motivated the use of displacement control rather than load control.

In the pull-off load case, a prescribed displacement was applied to all nodes in the top surface of the web, pulling them vertically upwards 10 mm (0.4”) or until failure. The pull-off fixture was modelled as two rigid and fully constrained surfaces with a sliding contact against the skin laminate, see highlighted components half-model shown in Figure 3.17.

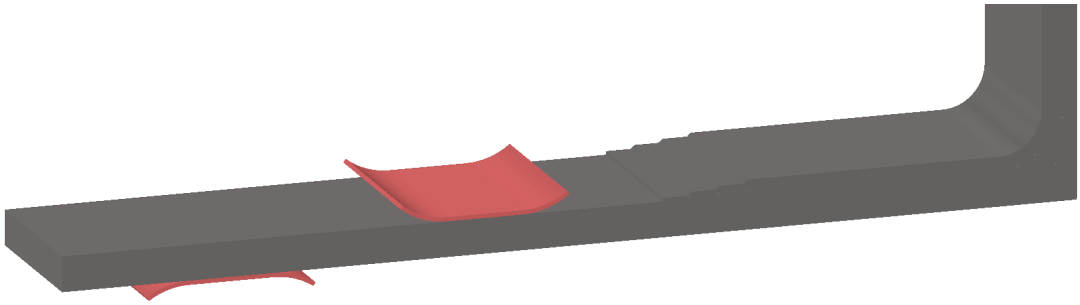

Figure 3.17: FEA model of pull-off fixture.

As mentioned in Subsection 3.6.2 the shear specimens were widened to 6" (152.4 mm) to reduce edge effects. However, as mentioned in Subsection 3.7.1, the width of the FEA specimens was limited to 1" (25.4 mm) due to the computational power available.

For the shear load case the skins were constrained by locking all translational degrees of freedom in the areas clamped by the test fixture presented in Subsection 3.6.2. As mentioned in subsection 3.7.1, the modelled webs were shortened to end 5 mm (0.2") above the top of each pi-joint, even though the lateral force from the shear test fixture is transferred to the web through a bolt pattern 1" (25.4 mm) above the top of the pi-joint. The prescribed displacement of the web was therefore initially applied to the nodes along the top surface of the shortened web which was deemed a reasonable simplification given that the shear force was still applied above the top of the pi-joint. However, this resulted in too large edge-effect for the simulations to provide any useful results.

In an attempt to reduce the edge-effects, the prescribed displacement was also applied to the nodes on the side of the web facing the loading direction. This was done to reduce the lever arm of the displaced nodes which contributes the bending moment in the modelled specimen. Applying the prescribed displacements along the entire side of the web is equivalent to using an infinitely stiff web and instead resulted in large singularities in the bottom corners of the clevis where the web meets the pi-joint. To avoid these singularities while still reducing the aforementioned leverage, the prescribed displacements on the side face were only applied to nodes down to 10 mm and 20 mm up from the bottom of the web respectively, see Figure 3.18. However, both of these intermediate configurations of boundary conditions still resulted in significant edge effects.

Initial Tsai-Wu failure for the shear load case consistently appeared in the edges of the web and the top corners of the pi-joint walls; before any damage was predicted in the root region or the interface between the pi-joint and the skin. This is the expected failure for a specimen that is not wide enough and therefore experience large tensions and compressions in the sides of the web due to the resulting moment from the load application points, as described in Subsection 3.6.2.

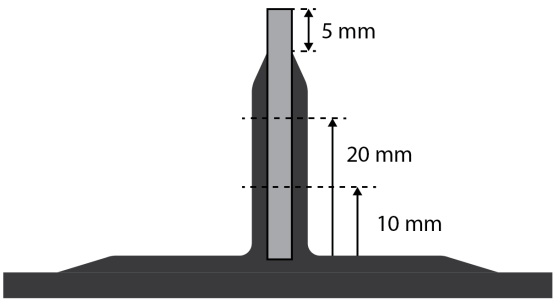

Figure 3.18: Illustrations of shear boundary conditions tested.

3.7.3 Benchmarking of cohesive elements

As mentioned in Section 2.3.2, cohesive elements can be used to predict crack initiations anywhere in a cohesive zone. Ideally these elements would be used between every single ply as to detect delaminations within each sub-laminate. However, as these elements are computationally expensive, their use was limited to the interfaces between sub laminates, and failures within the sub-laminates were predicted using the Tsai-Wu failure criterion without regard to interlaminar failures. Examples of the cohesive zones are the interface between skin, pi-preforms, and web, as well as the interfaces against the filler regions of solid resin.

As mentioned in Section 2.3.2, CZM is strongly dependent on the mesh size of the cohesive elements and the elements they are in contact with. Through testing varying mesh sizes in the LU-style pi-joint model, it was found that the smallest element size that could be used and solved within a reasonable time (less than 2 hours) was 0.5 mm (0.02") for the laminates and 0.25 mm (0.01") for the cohesive elements. The LU-style pi-joint model was used for this test as this is the most geometrically complex model and hence contains the most elements.

At this mesh size, the FE solution would not converge without the use of Viscous Energy Dissipation (VED). To validate the mesh size in combination with varying amounts of VED, a benchmarking study was performed using the models and properties presented in a paper by Harper and Hallett [41]. The graph presented in Figure 3.19 shows the simulated load displacement curves for pure mode I fracture with VED of 0.025% - 1% compared to the theoretical solution using corrected beam theory. As can be seen, the 0.025% damped solution follows the behaviour of the cohesive zone during the crack propagation albeit slightly stiffer. Lower viscous damping would have been beneficial; however, 0.025% damping was the least amount of damping required for the solution to converge.

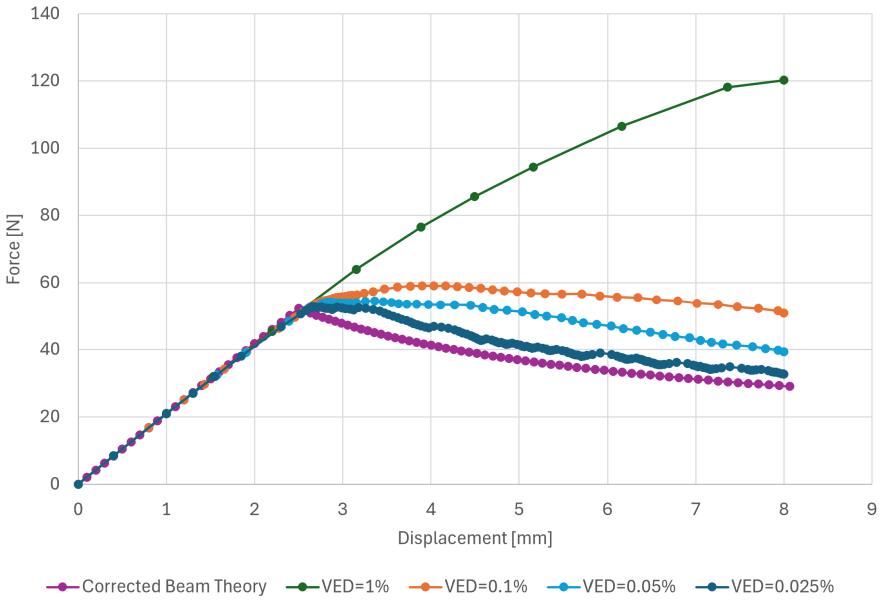

Figure 3.19: Load-displacement curve for mode I fracture with varying viscous damping.

The graph in Figure 3.20 compares the load response of the 0.025% damped solution to the theoretical solution. This shows that the damped solution underestimates the stiffness of the cohesive elements during the cohesive initiation by less than 4% error. Meanwhile, it overestimates the stiffness between 10%-15% during the cohesive propagation.

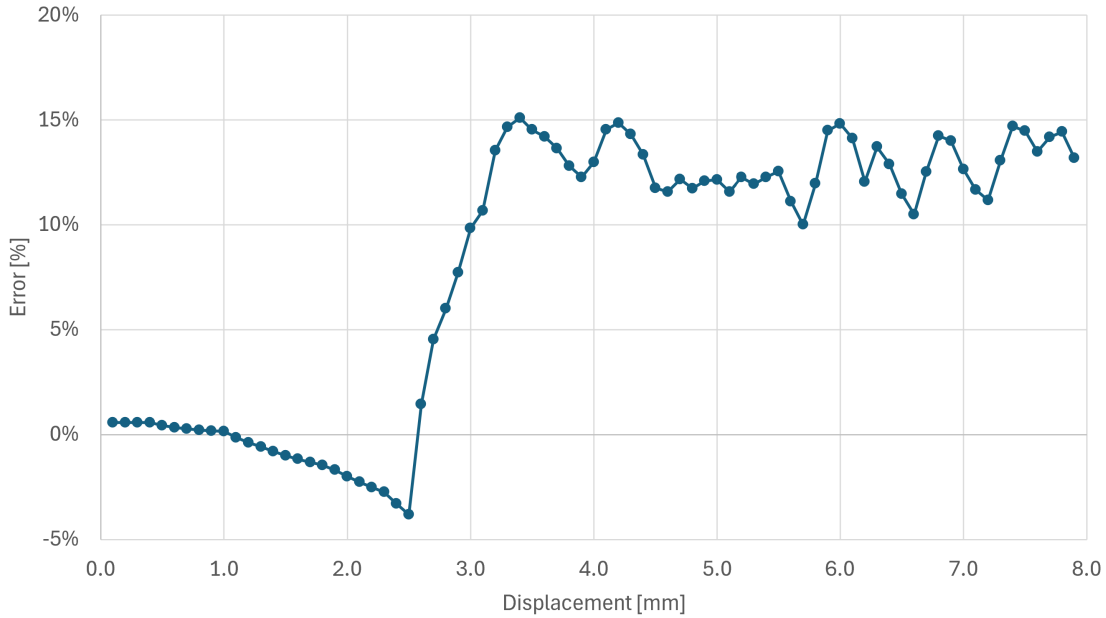

Figure 3.20: Error of viscous damped solution compared to theoretical solution.

This was deemed acceptable as the models primarily aim to predict the behaviour

of the pi-joint up to cohesive failure and not the cohesive propagation. The final mesh size was therefore 0.5 mm (0.02") for the laminates and 0.25 mm (0.01") for the cohesive elements with a VED of 0.025%. All pi-joint models were initially simulated with larger 0.5mm (0.02") cohesive elements in the entire interfaces between sub-laminate. Based on indications of where damage initiates the cohesive zones were reduced to more localized regions with the finer 0.25mm (0.01") mesh size.

As cohesive elements were used both in the co-cured interface between the pi-joint and the skin, as well as in the secondary bonded interface between the pi-joint and the web, two different sets of fracture toughness and interface strengths were needed. The interface strength τ_I of the co-cured interface was defined as the transverse tensile strength of the proprietary HiTape + HiFlow laminate properties, and for mode II and III it was defined as the interlaminar shear strength. Due to a lack of physical test data for the fracture toughness of the HiTape + HiFlow material, the fracture toughness was defined based on a similar composite material, IM7/8552. The parameters used were $G_{Ic} = 0.212\text{kJ/m}^{-2}$ and $G_{IIc} = G_{IIIc} = 0.774\text{kJ/m}^{-2}$ [35].

For the secondary bonded interface using the FM300-2 adhesive, the mode I interface strength as well as mode I and II fracture toughness were defined based on a research paper by Jokinen et al [6], see Table 3.4. The remaining interface strength for mode II was defined as the lap shear strength from the material datasheet [46].

Property	**Value**
G_{Ic}	1.038kJ/m^{-2}
$G_{IIc} = G_{IIIc}$	4.897kJ/m^{-2}
τ_I	34.49 MPa
$\tau_{II} = \tau_{III}$	40.7 MPa

Table 3.4: Material properties used for FM300-2 cohesive elements.

3.7.4 L-style pi-joint

The L-preforms were modelled ply by ply with the theoretical inner radius of 0.25" (6.35 mm) and the filler region in the root was modelled as solid elements with the isotropic material properties of the HiFlow 1078-1 resin as defined in the product datasheet [24]. The cohesive zones extend 5 mm (0.2") out from the ends of the radius as indicated by the dashed black lines in Figure 3.21.

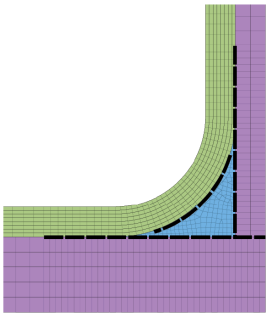

Figure 3.21: Illustration of cohesive zones in the L-style pi-joint FEA model.

3.7.5 LU-style pi-joint

The L-preform for the LU-style pi-joint was modelled using the same method as used for the L-style pi-joint with the only difference being the stacking sequence and ply-drop order as described in Subsection 3.2.4.

To model the U-preforms, cross-sectional images of physical specimens were used as reference. This was needed as the U-preform tended to distort within the root region during the infusion process. Figure 3.22 shows a side-by-side comparison of plies in a physical LU-style specimen and the FEA modelled plies used in the simulations.

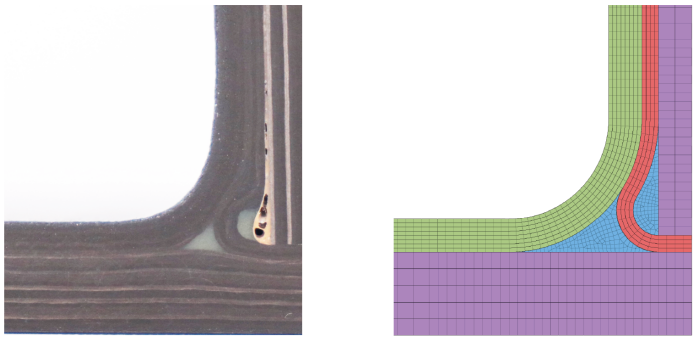

Figure 3.22: Comparison of physical specimen and FE model of LU-style pi-joint.

Similarly to the L-style pi-joint, cohesive elements were used near the root of the pi-joint in all interfaces between sub laminates and the filler regions, see Figure 3.23.

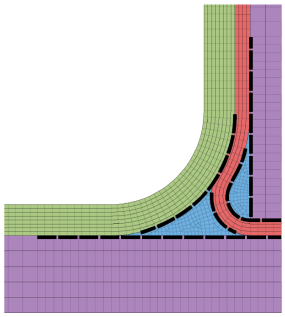

Figure 3.23: Illustration of cohesive zones in the LU-style pi-joint FE model.

3.7.6 3D woven pi-joint

The 3D woven pi-joint are woven using fibres in the 0- and 90-directions. This complex weaving was simplified as stacked 2D woven plies with the same interlaminar properties as the in-plane properties. Each solid ply was homogenized as two UD plies, one in the 0-direction and one in the 90-direction.

Figure 3.24 illustrates the structure of all plies, the thickness of the 3D woven pi-joint is equivalent to eight plies in the base and four plies in the walls. To simplify the continuous fibre transition from the base to the walls, the two topmost plies of the base curves up along the walls forming a combined stack of four plies.

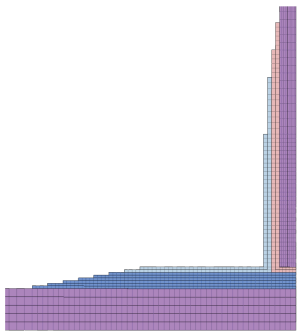

Figure 3.24: FE model highlighting the plies of the 3D woven pi-joint.

Initial simulations showed that cohesive zones were necessary in the entire interface between the pi-joint and the skin whereas the cohesive zones between the pi-joint and the web could be reduced, see Figure 3.25.

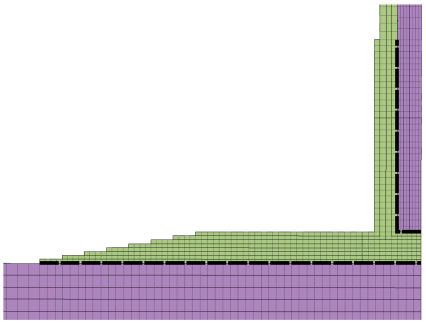

Figure 3.25: Illustration of cohesive zones in the 3D woven pi-joint FE model.

3.7.7 Braided pi-joint

The braided preforms consist of both 0° and ±45° fibres braided as a single ply. The distribution of these fibres is 50/50/0, meaning that 50% of the fibres is in the 0-direction and 50% in the ±45-direction. For the FE modelling, this braid was simplified as four UD plies homogenized, two in the 0-direction, and two in the ±45-directions.

The bottom of the sandwich panel, including the core material, is bonded to the pi-joint. However, as the bonded surface area of the core edge is minimal and the strength of the core in-plane is very low, the FE model was simplified to exclude the core material and only account for the bond between the pi-joint and the web laminate. This was deemed an acceptable simplification as both load cases are based on forces along the mid-plane of the web without regards to the out-of-plane clamping force from the fixtures.

As mentioned in Subsection 3.7.3 cohesive zones were initially modelled for the entire interface between the pi-joint and the skin, as well as the web. These were then reduced to only extend 0.5” (12.7 mm) from the root of the pi, see Figure 3.26.

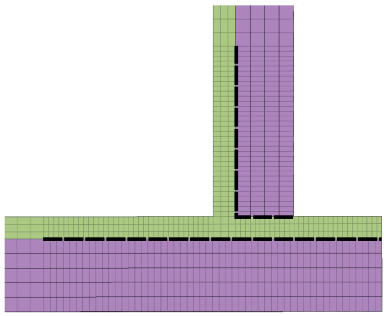

Figure 3.26: Illustration of cohesive zones in the braided pi-joint FE model.

4

Manufacturing

This section describes the used manufacturing processes in further detail as well as the difference in manufacturing process between the four configurations. It explains the variations in fibre layup for the skins, webs, and both L- and U-shaped preforms. Additionally, it presents the hot draping method used to shape the L- and U-preforms into their final shape. The infusion process is described in detail for the web panels, as well as for the co-curing of the pi-joint and skin.

4.1 Fibre layup

All test panels such as skins, webs, U-preforms and L-preforms were laid up using an AFP machine with an eight-spool head from the manufacturer Electroimpact. To minimise layup time, multiple web panels were nested into larger master panels from which subpanels were cut out after resin infusion. Similarly, the skin panels were nested to larger master panels, however, the individual skin panels were cut out before infusion due to size limitations of the infusion setup.

4.2 Hot draping L- and U-preforms

After the fibres were laid up, the L- and U-preforms were hot draped into shape. The L preforms were hot draped over an aluminium square tube with rounded corners matching a 0.25" (6.34 mm) radius to form the required 90° bend, whereas the U-preforms were hot draped over the edge of a 0.2" (5.1 mm) thick steel sheet.

The preforms were draped over the tools at room temperature by vacuum bagging them according to the schematic in Figure 4.1. The fibres were then relaxed into shape by ramping up the oven with 3°F/minute up until 250°F(121°C) and held there for 10 minutes before quickly ramping back down to room temperature. The vacuum was maintained until the thermocouple showed no more than 90°F(32°C) to minimise spring back.

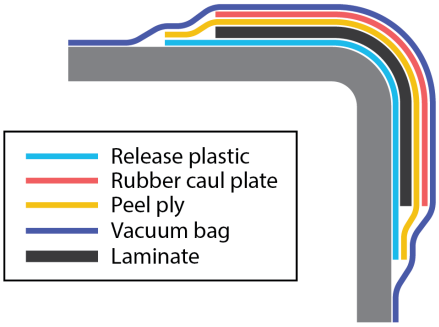

Figure 4.1: Schematic used for hot draping.

The thermoplastic veil on the dry fibres tend to stick to the tooling surface during hot draping despite using release agent, and therefore the layer of release plastic was added between the fibres and the tooling. A layer of peel-ply on top of the fibres acted as a flow media for the air, assuring even distribution of pressure. Thermocouples were positioned between the laminate and the tooling to monitor the preform temperatures in the oven, but since these created imprints they were only used in the trimming regions by the edges of the preforms. To avoid fibre wrinkling on the outside of the preforms caused by the vacuum bags, thin rubber caul plates were used between the peel-ply and the vacuum bag.

4.3 Web manufacturing

The web panels were infused using a spiral resin inlet suspended in a pleat along the centreline of the panel. This was done to test the centre-out infusion method planned for the pi-joints. Not suspending the spiral tube in a pleat would result in an imprint on the surface causing potential defects. Figure 4.2 illustrates the full vacuum bagging schematic used for the web panel infusions.

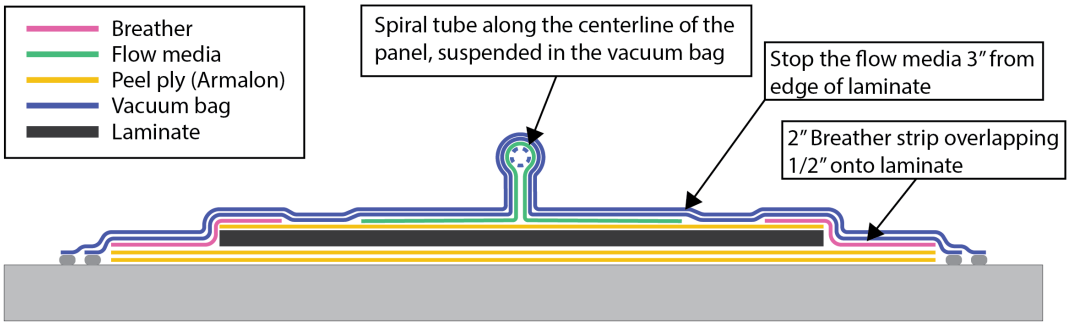

Figure 4.2: Schematic used for vacuum bagging web panels.

Multiple vacuum ports along the perimeter of the panel were used to individually

close of the vacuum as the resin flow-front progressed, see Figure 4.3.

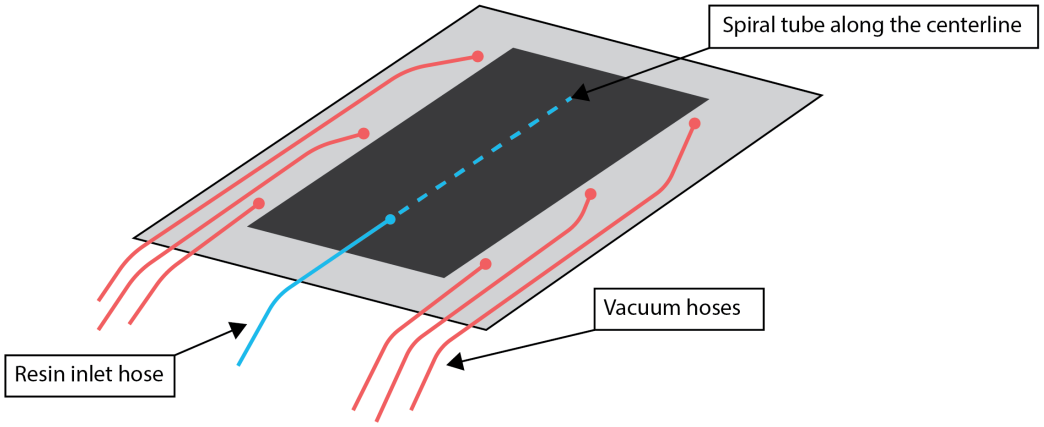

Figure 4.3: Schematic used to positioning of vacuum and resin lines for web infusion.

After infusion the web panels were cut to final dimensions using a composite plate saw. As peel-ply was used on both sides of the web laminate during the infusion there was no need for additional surface preparation before the secondary bonding process.

4.4 Co-curing the pi-joints

The co-curing process of the pi-joint to the skin involves multiple manufacturing steps, each with specific tolerance requirements. These steps are described more in detail in each subsection starting with the design of the clevis gap and the importance of the tolerance. The infusion setup is described in further detail to better understand how the setup and process were designed.

4.4.1 Clevis gap tolerance

Film adhesives generally have poor gap-filling properties since they are manufactured with a controlled amount of resin per unit area and tend to have higher viscosity during curing compared to paste adhesives. Despite these disadvantages of using film adhesive, it was deemed to require less testing to achieve a strong and repeatable bond. Therefore, it is important to have good control over the gaps between the web and the insides of the pi-joint clevis. To avoid the need for tight thickness tolerances on the web, the cured webs themselves were used as the tooling for the pi-joint clevis. By wrapping the webs in layers of vacuum bag and peel ply, the clevis width cures to the combined thickness of the web and the stacked consumables. To achieve the 0.013” (0.33 mm) nominal thickness of the adhesive film, two layers

of peel ply and one layer of vacuum bag was used. A layer of peel ply inside the vacuum bag kept the bag from sealing against the web trapping air bubbles, and another layer outside the bag is used to leave a rough surface inside the pi-joint clevis for better bonding.

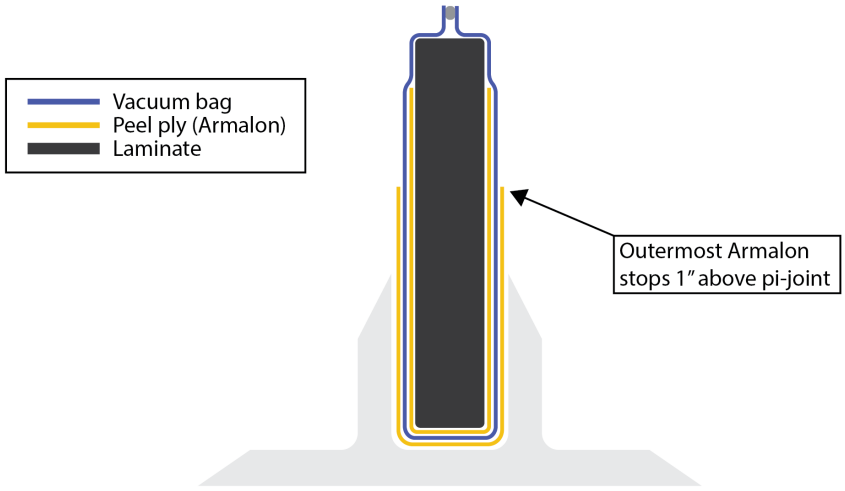

Figure 4.4: Schematic used for wrapping web prior to co-curing.

4.4.2 Infusion setup

There are many important factors to consider when resin infusing composites and one such is the distance the resin must flow before it begins to gel. To minimise the distance that the resin needs to flow, a spiral tube along one side of the web was used as resin inlet being strategically close to the centreline of the test panels, see Figure 4.5. The reason for only having an inlet on one side of the web is to avoid any colliding flow-fronts as trapped air bubbles leave voids within the laminate. Figure 4.6 illustrates the intended flow directions.

As the resin reached the three outlet edges at different times multiple vacuum lines were used to allow each line to be closed off individually. Figure 4.5 illustrates the placement of resin inlet and vacuum lines.

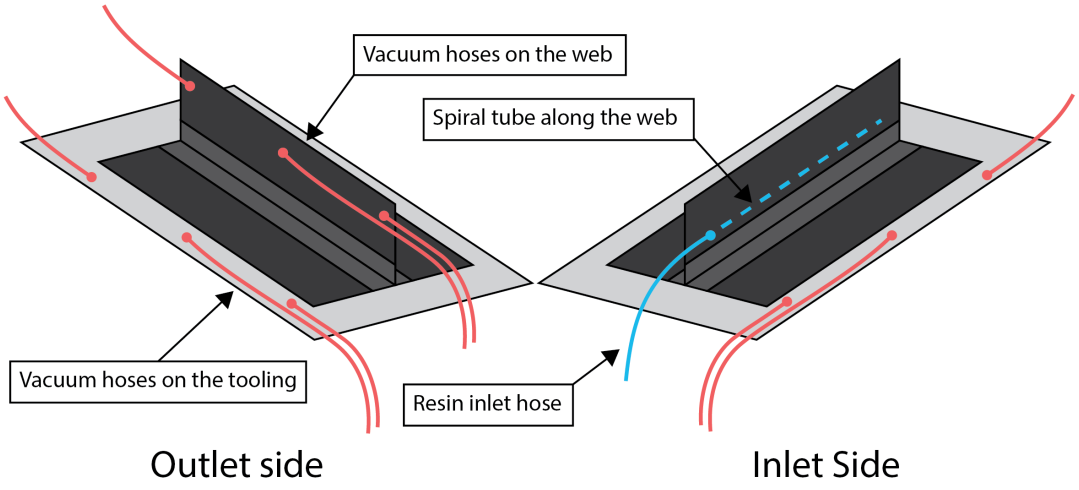

Figure 4.5: Schematic used to positioning of vacuum and resin lines for co-curing.

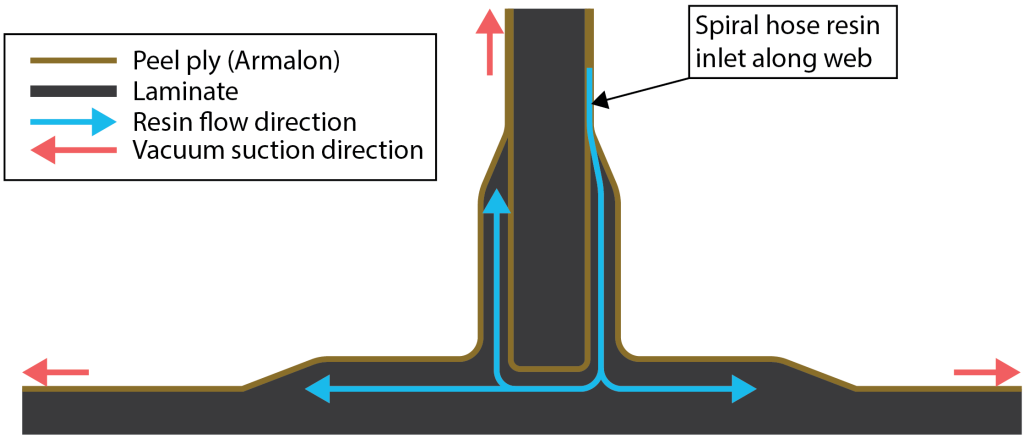

Figure 4.6: Illustration of resin flow directions during co-curing.

By slowing down the flow front before it reached the edge of the panel, the resin had more time to flow through the entire thickness of the laminate rather than flowing along the top-surface without saturating. This was achieved by ending the flow media 3" (76.2 mm) from the edges of the skin laminate to slow down the flow closer to the vacuum ports, ensuring the entire laminate is saturated before resin reaches the outlet. Figure 4.7 illustrates the complete vacuum bagging schematic used for all pi-joints infusions (excluding the corner pleats).

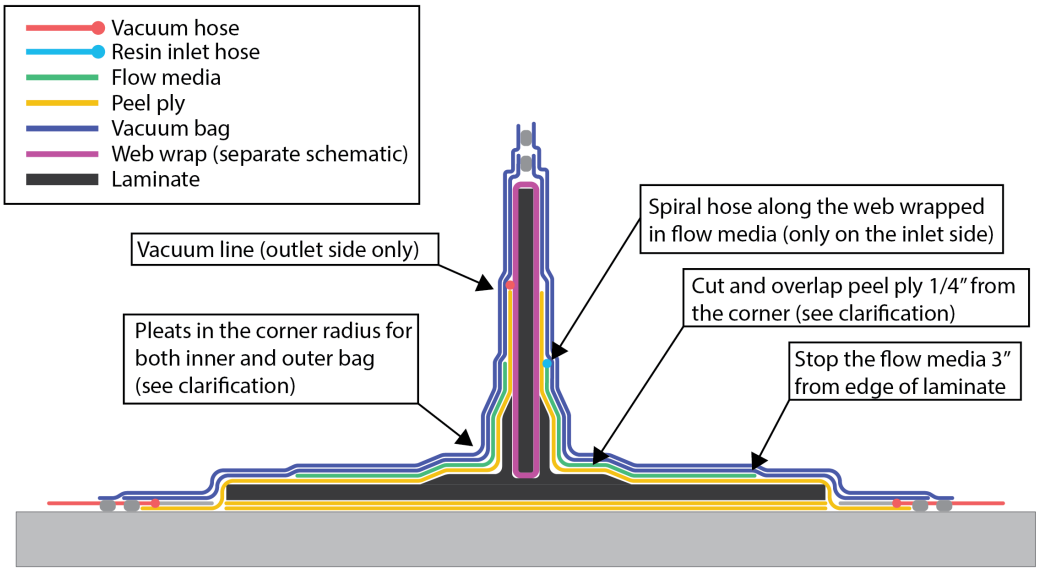

Figure 4.7: Schematic used for vacuum bagging the co-curing.

Any bridging in the corners of the pi-joints would result in a lack of vacuum pressure in these critical regions. To help the vacuum bag and peel-ply to slide against each other rather than stretching, the peel-ply was cut and overlapped, and the vacuum bag was pleated. Both methods cause slight imprinting on the cured surface, so to avoid any defects in the radius of the L-preforms the peel-ply overlap was positioned about 0.25” (6.35 mm) outside the corner radius. Similarly, the vacuum bag was pleated above and below the corner radius of the L-preforms, while the sharp corners of the braided and the 3D woven preforms only used a single pleat.

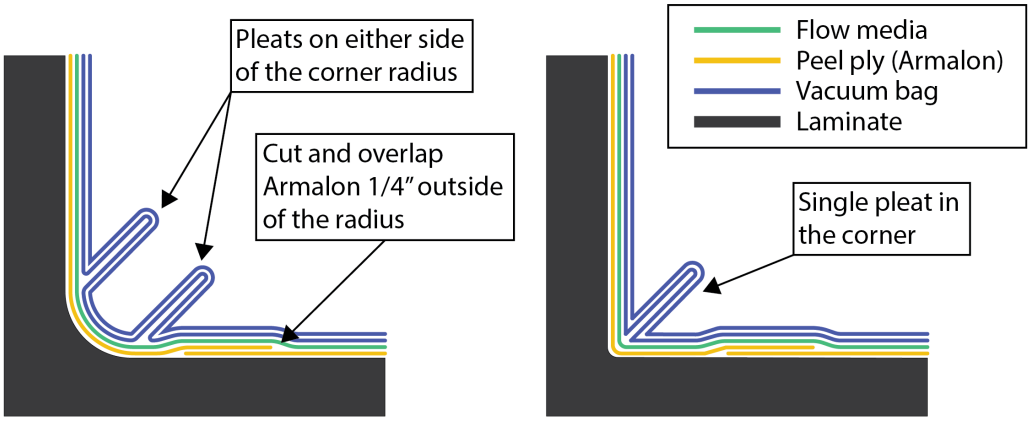

Figure 4.8: Schematic used for pleating the vacuum bagging for the co-curing.

4.4.3 Manufacturing fixture

The webs were held in place during the infusion by the vacuum bag as illustrated in Figure 4.7, however, a fixture of extruded aluminium profiles was needed to guarantee the webs were kept vertical until cured, see Figure 4.9. The web was clamped to the fixture using C-clamps on either ends and the fixture itself was clamped to the aluminium tooling.

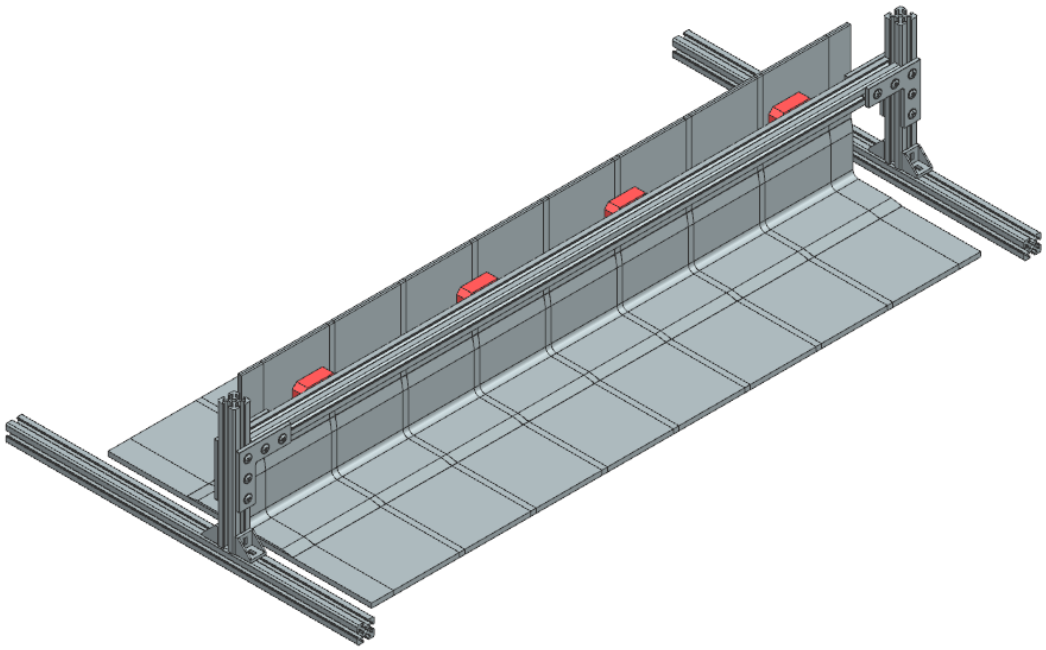

Figure 4.9: CAD render of fixture used to position webs during co-curing.

4.5 Bonding the webs

The adhesive film was wrapped around the lower section of the webs before the webs were inserted into the pi-joints. Strips of Teflon-coated paper were used to protect the film adhesive from ripping on the sharp top edge of the pi-joints during the insertion. When the web was inserted into the pi-joint, the strips were removed by pulling them out while keeping the web in place. The bonding was cured using the manufacturer's recommended curing cycle of 250°F for 90 minutes but without external pressure. Thermocouples pressed against the ends of the film adhesive were used to monitor and control the temperature of the curing cycle.

5
Inspection and testing

This section presents how the physical test specimens were inspected to validate that they did not contain any major manufacturing defects, as well as how a separate specimen containing known defects were used to compare inspection methods. Additionally, this section presents the testing matrix for the destructive testing including the conditions under which the specimens were tested.

5.1 Physical test specimen inspections

Both webs and skins were inspected using pulse-echo ultrasonic as C-scans to check the quality of the resin infusions. The webs were inspected separately prior to being bonded into the pi-joints as to ease the inspection process. Once the skins were co-cured, and the webs bonded in place, the skins were inspected from the bottom side.

5.2 Defect specimen inspection

As mentioned in the aim of the project, one outcome was to evaluate NDI methods based on their suitability for inspecting pi-joints in large aircraft structures. When pi-joints are used in closed structures such as wings, the accessibility can be limited, and the joints would need to be inspected from the outside of the skin.

The test specimen used for evaluating different NDI techniques contained three intentionally embedded defects listed below. These defect locations were selected to simulate regions with elevated risk to Foreign Object Debris (FOD) contamination.

- Missing tows on one side of the pi-joint.
- Flash tape within the bonded joint line.
- Voids in the bondline.

The three inspection methods selected to be evaluated are active thermography, pulse-echo ultrasonic, and X-ray CT. Based on the theory presented in Subsection 2.6.3, active thermography was excluded due to its shallow inspection depth. To evaluate the ultrasonic pulse-echo, a C-scan was generated by scanning the underside of the skin in a sweeping pattern with a resolution of 0.02” (0.5 mm). The resolution required for X-ray CT scanning depends on the objective of the inspection.

Since the primary goal was to use the X-ray CT-scan as a baseline for evaluating the pulse-echo UT, a resolution of 76 μm was deemed sufficient as it significantly finer than the 0.02" (0.5 mm) resolution used for pulse-echo UT. However, there are defects smaller than 76 μm and determining the exact size and shape of such defects would require an even finer resolution.

5.3 Destructive testing

As mentioned in Section 1.4, the physical testing will be carried out as a separate project. However, the following section outlines the proposed test plan.

For the pull-off load case, three specimens of each pi-joints are to be tested in cold temperature of -65°F(-54°C) and three specimens in room temperature of 70°F(21° C). For the shear test, five specimens are to be tested in room temperature and another five specimens in elevated temperature of 180°F(82°C), see Table 5.1. This is summarized in the test matrix presented in Table 5.1. The temperatures for colder and elevated test are based on the temperatures used for material characterisation by NCAMP [36].

Table 5.1: Test matrix.

Load case	Cold temp -65°F (-54°C)	Room temp 70°F (21°C)	Elevated temp 180°F (82°C)
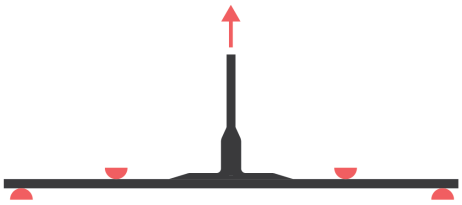	3	3	-
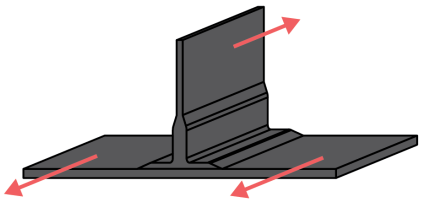	-	5	5

6
Results

This section presents results from FEA simulations, manufacturing challenges and solutions together with NDI methods and cost comparisons. It highlights problems within the FE models and the result from the simulations. Additionally, this section presents challenges and solutions to several manufacturing problems which occurred, and how well different NDI methods works for inspecting pi-joints. The cost comparison presents normalized values for the price of each pi-joint, the manufactured pi-joint prices include costs such as material cost, technician cost but not the deprecation cost.

6.1 FEA results

This section presents the FEA results for all four types of pi-joints, these results include both the Tsai-Wu failure index of the plies and the cohesive failure index of the cohesive zones for varying displacements. Due to uncertainties in the material parameters the result for each pi-joint remains inconclusive whether the intralaminar (Tsai-Wu) or interlaminar (cohesive) failure will occur first; and therefore, the two types of failures will be discussed separately.

Due to the problems related to the shear models discussed in Subsection 3.7.2 it was not possible to obtain reasonable or useful simulation results for the shear load case and will therefore not be presented.

6.1.1 Pull-off load case

The estimated failure loads in the pull-off load case are summarized as a bar graph in Figure 6.1 and the behaviour of each pi-joint configuration is further detailed in the following subsections. As mentioned previously, the material data for both the laminates and the cohesive interfaces are based on approximations and preliminary test data. Hence, it is uncertain whether the Tsai-Wu failures or the cohesive failures will occur first, given that the strength of either one material could be over/underestimated. Therefore, when comparing the relative strengths of the different pi-joint configurations in Figure 6.1, the Tsai-Wu and cohesive results have been normalized separately. The normalization was done by diving all the Tsai-Wu failure loads (both initial and ultimate) by the maximum predicted Tsai-Wu failure load of the 3D woven specimen (the highest failure load of all). The same process was used for

normalizing the cohesive failure loads but these were divided by the cohesive failure load of the 3D woven specimen.

Each bar in the graph represents estimated initial and ultimate failure loads for each pi-joint configuration. The initial failure load is defined in the same way for both cohesive and Tsai-Wu failure as the load at which any element has reached Tsai-Wu failure or cohesive failure respectively. However, ultimate failure is defined in two different ways for the two failure modes. Ultimate cohesive failure is defined as the load where the remaining cohesive elements fails simultaneously, and the simulation shows complete separation. Whereas ultimate Tsai-Wu failure is defined as the load at which Tsai-Wu failure has occurred through the entire thickness of a laminate, at which the joint is deemed to have failure completely. The ultimate Tsai-Wu failure load will be a significant overestimation as the models do not account for loss of stiffness in elements that have reached Tsai-Wu failure. The true ultimate Tsai-Wu failure load should therefore be between the initial and ultimate failure loads indicated in the graph, but much closer to the initial failure load.

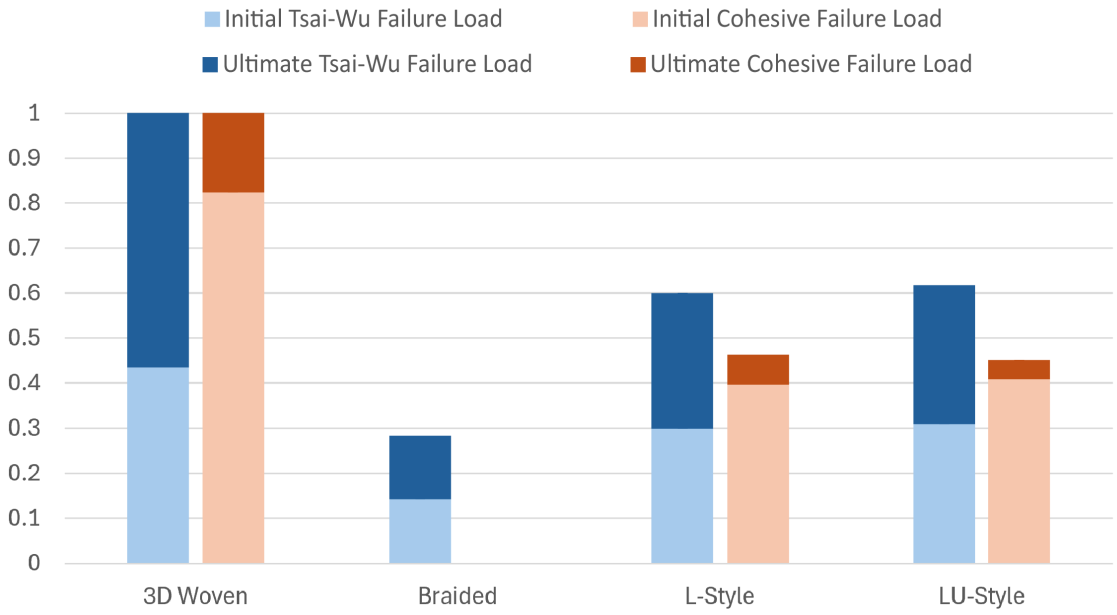

Figure 6.1: Comparison of normalized failure loads for pi-joint configurations in pull-off.

As explained in Subsection 3.7.2, the pull-off load case was modelled using a prescribed displacement on the top-edge of the web. Hence, all references to prescribed displacements in the following sections refer to the displacement of the top-edge of the web.

The figures in the following subsections present the Tsai-Wu failure index and the cohesive damage index for four load steps of interest. Both the Tsai-Wu failure index and cohesive damage index range from 0 to 1 represented as colour scale from blue

to red. The four load steps presented are:

1. Initial Tsai-Wu failure, in any ply.
2. First load step with Tsai-Wu failure through the entire thickness of any preform, deemed to result in ultimate failure.
3. Initial cohesive damage.
4. Last load step before the ultimate failure of the cohesive zone, complete disbond.

6.1.2 3D woven

For the 3D woven pi-joint, initial Tsai-Wu failure appears in the root of the pi-joint where the pi-joint clevis meets the pi-joint base, as shown in Figure 6.2a. However, Figure 6.2b shows that the 3D woven preform also experience high stresses in the tapering of the preform thickness, potentially making it more prone to the peel-failures from large skin deformations described in Subsection 3.6.1.

This peeling effect can be seen in Figure 6.3c where the cohesive damage initiates by the outer edge of the pi-joint preform. This was the only pi-joint configuration to experience cohesive failure initiating from the outer edge and propagating inwards rather than initiating in the root region. The crack opening grows steadily until the load step shown in Figure 6.3d, upon which the remaining cohesive zone fails nearly instantaneous, resulting in complete separation of the pi-joint from the skin.

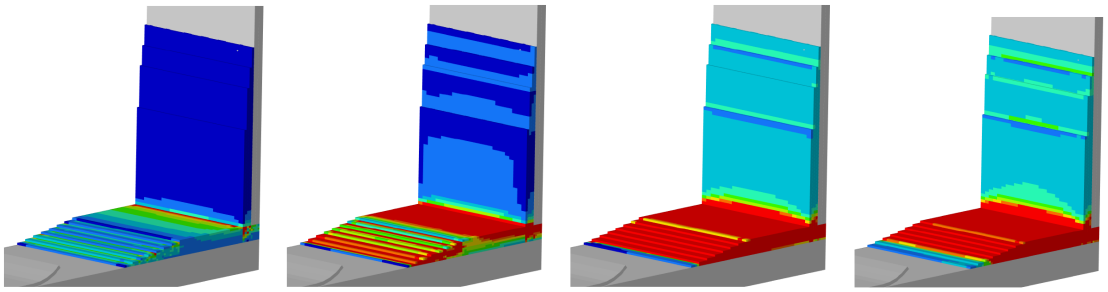

(a) 1.2 mm (0.05”) **(b)** 2.8 mm (0.11”) **(c)** 4.8 mm (0.19”) **(d)** 6 mm (0.23”)

Figure 6.2: Tsai-Wu failure index of 3D woven pi-joint during pull-off.

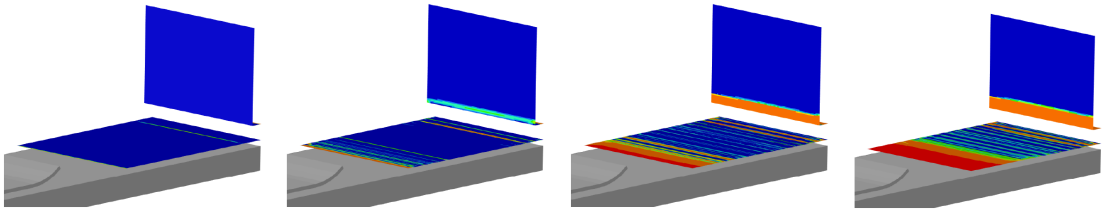

(a) 1.2 mm (0.05”) **(b)** 2.8 mm (0.11”) **(c)** 4.8 mm (0.19”) **(d)** 6 mm (0.23”)

Figure 6.3: Cohesive failure of 3D woven pi-joint during pull-off.

6.1.3 Braided

Similarly to the 3D woven pi-joint, the initial Tsai-Wu failure occurs in the root region of the pi-joint, see Figure 6.4a. However, due to the lower stiffness of the braided preforms base and its large size, the stresses gradually decrease to very low stresses by the edges of the pi-joint. Hence, any cohesive failure would most likely be limited to the root region. As shown in Figure 6.5, the braided pi-joint configuration did not experience any cohesive failure with up to 12 mm (0.47”) of prescribed displacement. This is most likely a consequence of the large sized braided specimens, which allows for larger displacement of the skin before any cohesive failure occurs. Additionally, the load transferred through the cohesive zone was less concentrated since the clevis of the braided pi-joint is significantly wider and therefore distributes the force over a greater area.

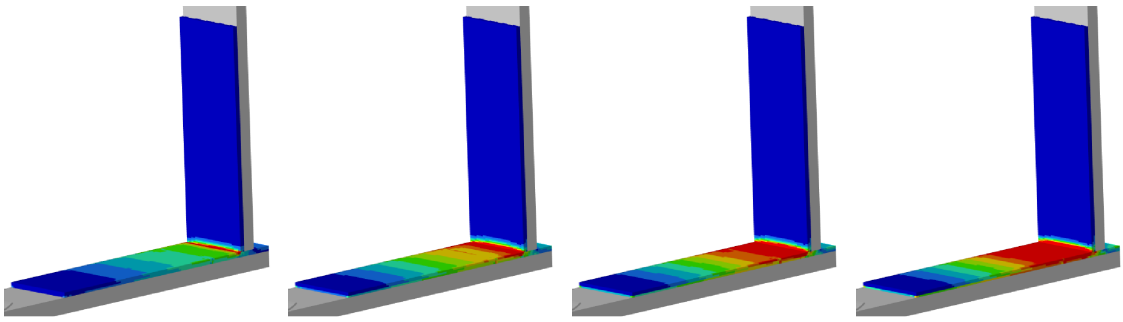

(a) 4 mm (0.16”) **(b)** 6 mm (0.23”) **(c)** 7 mm (0.27”) **(d)** 8 mm (0.31”)

Figure 6.4: Tsai-Wu failure index of braided pi-joint.

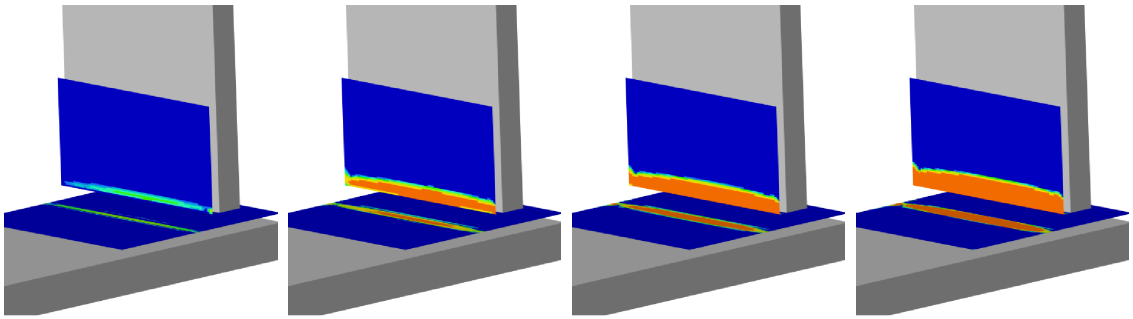

(a) 4 mm (0.16”) **(b)** 6 mm (0.23”) **(c)** 7 mm (0.27”) **(d)** 8 mm (0.31”)

Figure 6.5: Cohesive failure index of braided pi-joint.

6.1.4 L-style

As opposed to the two commercial pi-joint configurations, the L-style pi-joint show more distributed stress throughout the preform due to its significantly larger corner radius, see Figure 6.6a. As the L-shaped preform is loaded in tension it will slightly straighten out, causing it to pull away from the filler region. This explains the initiation of cohesive damage that can be seen in the middle of the radius at 7 mm (0.27”) displacement, see Figure 6.7c. The effect of the plies in the corner radius being forced to slightly straighten out could potentially cause delaminations within the laminate in this region which would require more detailed simulation models using cohesive zones between each ply.

Additionally, the less stiff filler region does not transfer much force to the cohesive zone between itself and the skin. Therefore, more stress is concentrated in the bonded interface between the bottom of the web and the skin; potentially making it more sensitive to voids in that bondline.

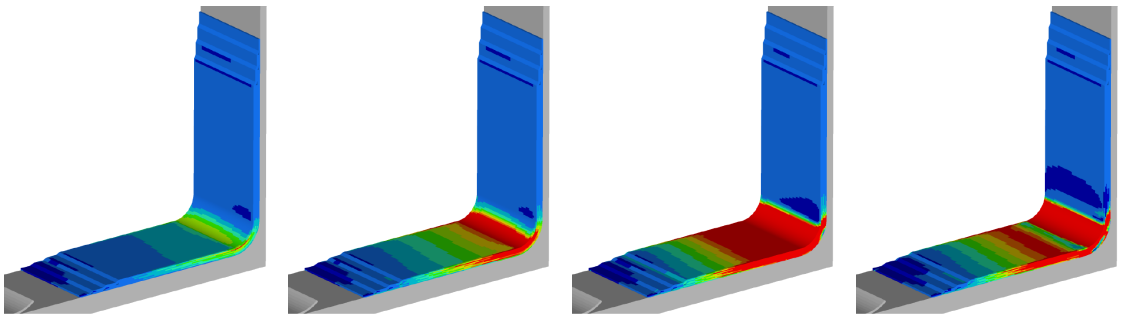

(a) 4 mm (0.16”) **(b)** 6 mm (0.23”) **(c)** 7 mm (0.27”) **(d)** 8 mm (0.31”)

Figure 6.6: Tsai-Wu failure index of L-style pi-joint.

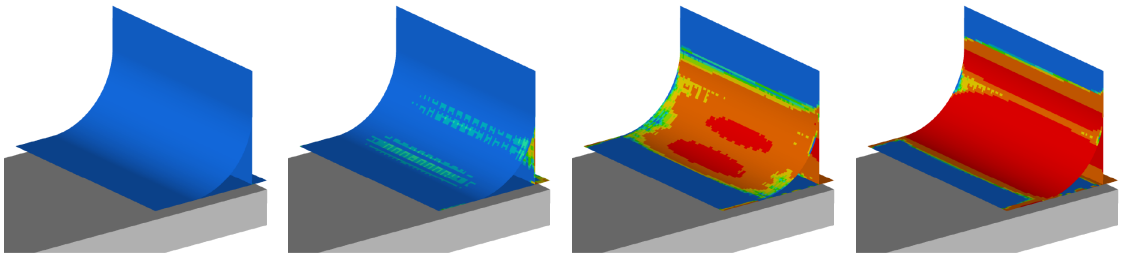

(a) 4 mm (0.16”) **(b)** 6 mm (0.23”) **(c)** 7 mm (0.27”) **(d)** 8 mm (0.31”)

Figure 6.7: Cohesive failure index of L-style pi-joint.

6.1.5 LU-style

Compared to the L-style configuration, it appears that the added U-preform does not make a significant difference. It appears to slightly improve the distribution of stresses between the web and the skin as the load is transferred through the bottom of the U-preform. However, as the U-preform does not conform very well to the web, but rather bulges out into the filler region, these fibres are not able to transfer significant loads from the bonded sides of the web down into the co-cured interface against the skin as indicated by their low stress. The cohesive failure therefore looks similar to the one observed in the L-style pi-joint configuration, initiating in the middle of the corner radius and growing outwards.

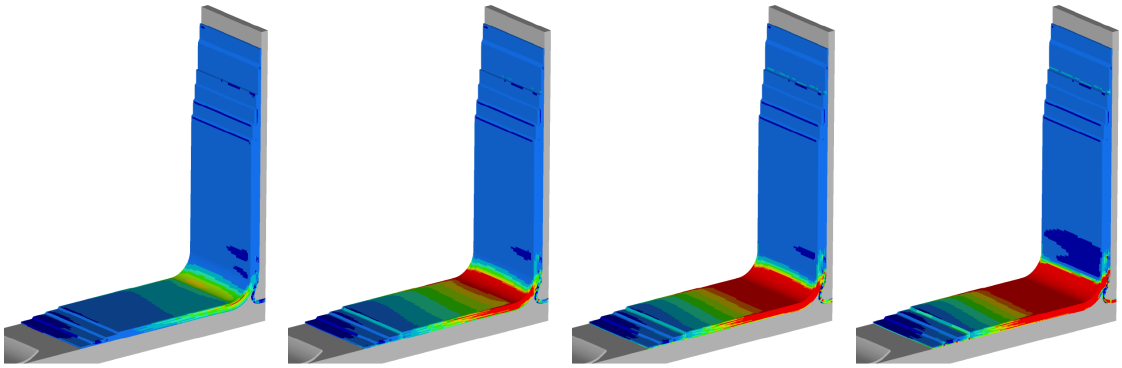

(a) 4 mm (0.16”) **(b)** 6 mm (0.23”) **(c)** 7 mm (0.27”) **(d)** 8 mm (0.31”)

Figure 6.8: Tsai-Wu failure index of LU-style pi-joint.

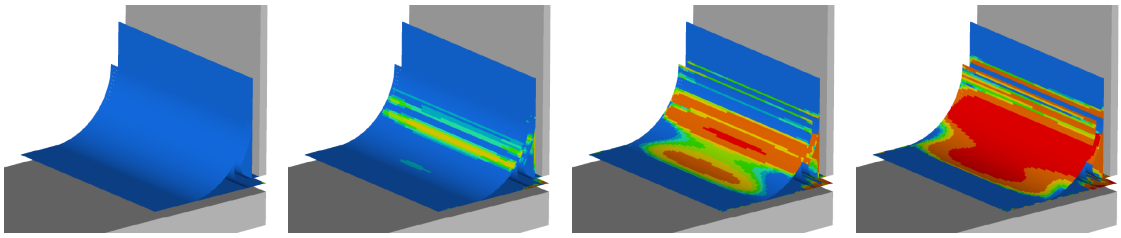

(a) 4 mm (0.16”) **(b)** 6 mm (0.23”) **(c)** 7 mm (0.27”) **(d)** 8 mm (0.31”)

Figure 6.9: Cohesive failure index of LU-style pi-joint.

6.2 Manufacturing

In this section results from all manufacturing steps are presented together with solutions to different challenges which have occurred along the manufacturing process. It highlights the challenges that comes with using an AFP machine, the shaping method of hot draping, infusion complex parts and bonding.

6.2.1 Layup

The layup of the skins and webs had no major issues during lay-up, the L- and U-preforms were more challenging. As mentioned in Subsection 3.2.3, some tows were designed to the minimum recommended length for the AFP machines to lay down. This resulted in difficulties of heating the thermoplastic veil to the correct temperature and making them more difficult to stick to the plies under. As a result, the handling of the L- and U-preforms became more challenging. However, the hot draping process melted the thermoplastic veil making the plies stick to each other. The tapered edges of the laminate being laid up to final dimensions without any trimming margin further complicated the process of going back and adding missing tows when tows jammed in the AFP head. The problem with missing tows were solved by taping down the previous laid tows and then go back and adding the missing tow, the tape was then removed.

6.2.2 Hot draping

Taping down one side of the L-preform and stretching the laminate over the edge of the hot draping tool resulted in minimal defects along the taped side but induced large areas of fibre wrinkling on the folded side, see Figure 6.10.

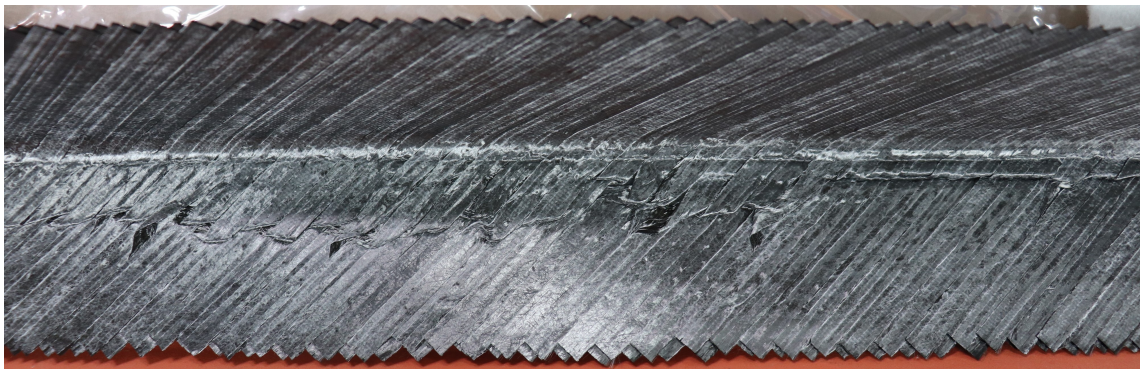

Figure 6.10: Large areas of fibre wrinkling due to the hot draping process.

By not stretching the laminate over the edge but bending if from the radius and outwards before taping it down the effect of fibre wrinkling was minimised but not eliminated, see Figure 6.11. There were no visible signs of wrinkling in the radius but rather a concentrated line of wrinkled fibres just outside the radius which was deemed to be acceptable.

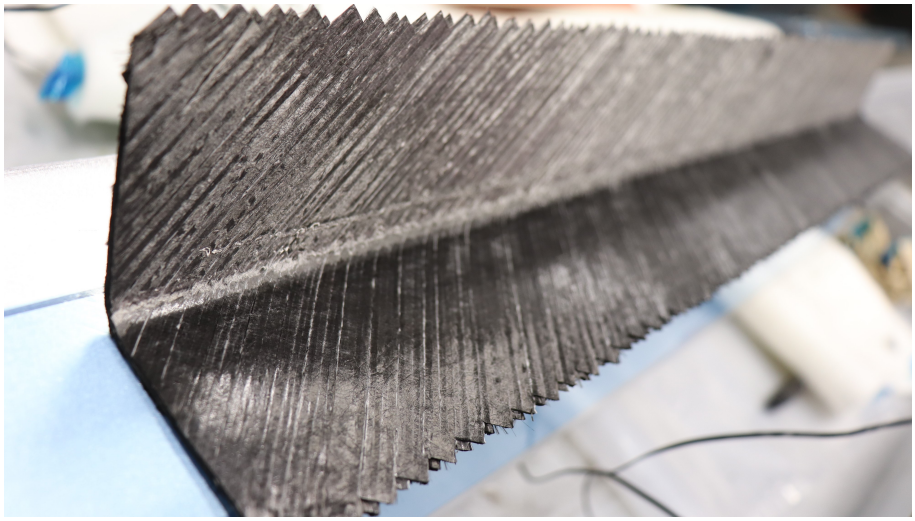

Figure 6.11: Hot draped L-preform with reduced wrinkling.

6.2.3 Infusion

The first infusion tests showed that the L- and LU-style pi-joint had significantly lower permeability compared to the 3D woven and braided pi-joints, resulting in dry spots on the outlet-side of the skins. This was solved by adding a second resin inlet in the corner pleats on the outlet-side which was not opened until the corners had fully saturated.

The 3D woven and braided pi-joints acted as flow media, allowing for a high resin flow and hence short infusion times. These infusions took approximately 40 minutes from opening to closing the resin inlet, whereas the L- and LU-style infusions varied

between 1,5-2 hours for the same sized panels. The vacuum ports were closed of one at a time as they started to pull resin out.

When debagging the L- and LU-style preforms, it was seen that the peel-ply on the outside of the web bag had stretched out leaving the resin to fill between the peel-ply and the vacuum bag causing a void in the noodle region, see Figure 6.12.

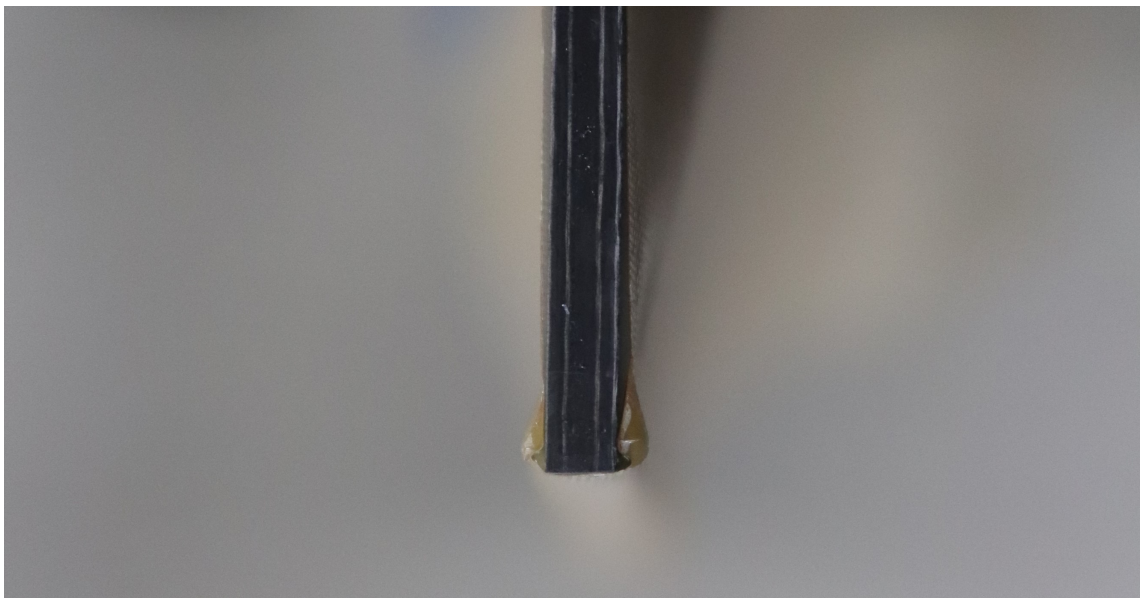

Figure 6.12: Resin-filled peel-ply from root region.

6.2.4 Bonding

The secondary bonding of the web to the pi-joint clevis using a film adhesive proved to be difficult. When preparing the web with the film adhesive it was seen that the film adhesive did not stick to the web as first though which made it more difficult to insert the web with the adhesive into the pi-clevis of the pi-joint. This was solved by heating the film adhesive using heat guns and then press the film adhesive against the web using debulking rollers. This also helped to overcome the very high friction forces occurring when sliding the film adhesive along the clevis walls. However, the Teflon coated paper in some cases proved to be difficult to get out especially from the 3D woven pi-joint where the clevis walls had warped inwards. In areas where the paper broke upon extraction, all pieces were laid out to confirm that no paper remained inside. Pushing the web all the way to the bottom of the clevis required additional force. This was done by using two large C-clamps, one in each end of the panel whilst the film adhesive was heated up using heat guns.

6.2.5 Manufacturing times

As mentioned in Subsection 6.2.3, the L- and LU-style pi-joints took longer to infuse for the same size panels as the 3D woven and braided pi-joints. The two AFP pre-

form configurations also had longer preparation times leading up to the infusions as they required layup and hot-draping. The manufacturing times presented in Figure 6.13 are based on the manufacturing of the physical test specimens in this project and could be reduced by optimizing the process and scaling it up for larger production runs. Although the L-preforms for both the L- and LU-style configurations took equally long to prepare, the LU-style configuration also required the preparation of the U-preform, hence the slightly longer manufacturing time. The 3D woven and Braided pi-joints required minimal preparation time other than infusion setup as these only needed to be cut to length.

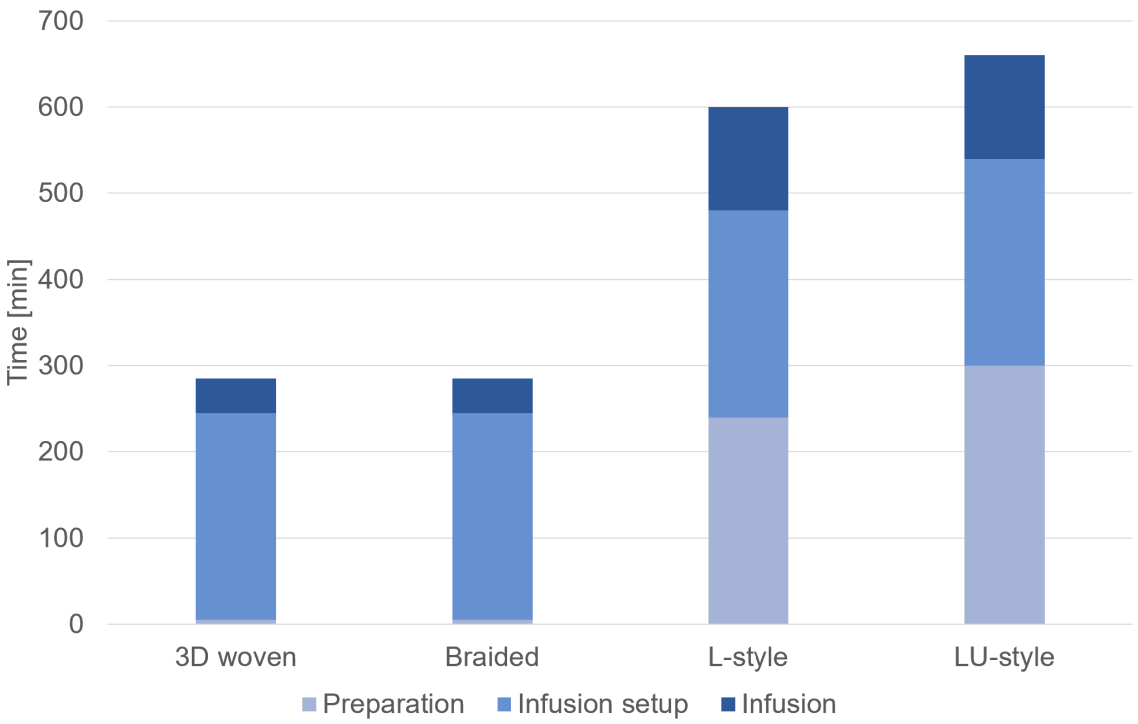

Figure 6.13: Manufacturing times of each pi-joint configuration including preparation and infusion.

6.3 Non-destructive inspection of defect specimen

The X-ray CT-scan of the defect specimen used as a baseline could clearly identify all three of the embedded defects as shown in Figure 6.14. The region with voids shown in Figure 6.14b extend approximately 1 mm (0.04”) from the face of the web.

Figure 6.15 shows that the pulse-echo UT C-scan captured from the bottom of the skin could successfully detect the missing tows as well as the embedded strip of flash tape wrapped around the bottom of the web. It can also be seen that the brightness of the centreline, created by the bottom of the web, vary along the length of the joint, indicating that the bond quality is not consistent. However, this only shows the small part of the secondary bond coplanar with the skin.

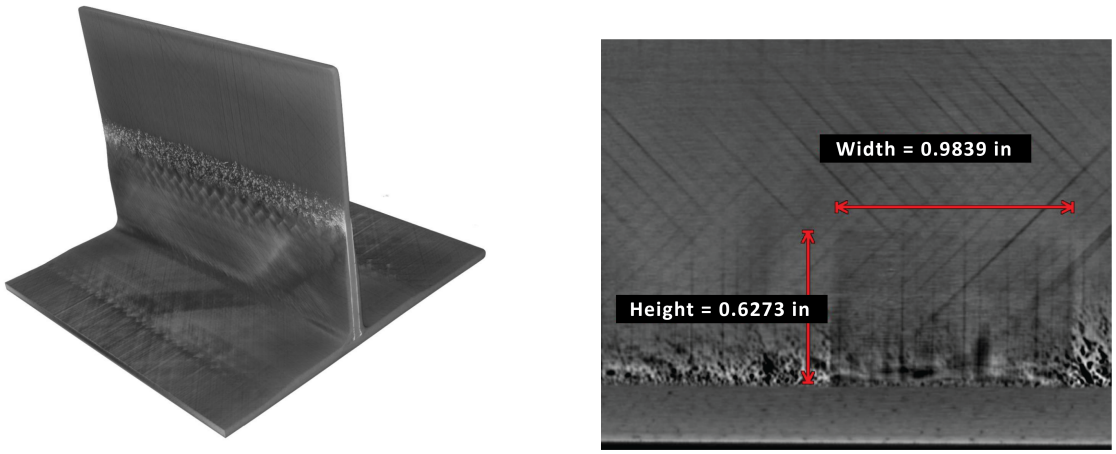

(a) Missing tows

(b) Flash tape and voids in the bondline

Figure 6.14: The three known defects detected by the X-ray CT-scan.

On both sides of the web, the measured return signal was much stronger as indicated by the dark regions in the image. This could be caused either by backscatter from large defects such as voids, or by large amounts of back-wall reflection caused by the emitted signal reflecting of the curved surfaces in the corner radius.

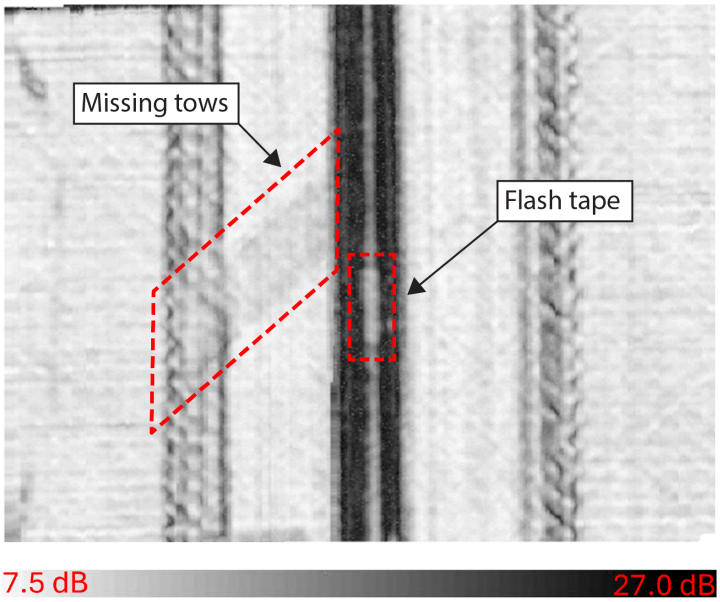

Figure 6.15: C-scan of defect specimen captured from the underside of the skin.

Comparing the inspection results of the corner regions, the voids only extend approximately 1 mm (0.04”) from the web according to the X-ray CT-scan, significantly shorter than the darker regions seen in the UT C-scan. This, combined with the

observation that the darker regions are consistent along the joint, even in areas with better bondline quality, means its more likely to be caused by back-wall reflection and persist even in a non-defect specimen.

6.4 Cost comparison of pi-joints

The cost comparison between the four pi-joint configurations is limited to the pi-joints themselves and does not consider any difference in the web- and skin panels. The factors considered for the cost estimation are:

1. *Material* cost, is calculated as the sum of fibre and resin cost. For the AFP preformed pi-joints both of these are calculated as the respective material weight for one meter of pi-joint, times the material cost per kilogram. For the commercial pi-joints, the fibre cost is based on quotes from the manufacturers.

2. *Layup cost* (AFP preforms only), was calculated based on the time taken to layup preforms multiplied by an hourly rate for AFP. This rate includes of operator cost, power consumption, maintenance, and machine depreciation based on estimates from Heart Aerospace. Not included in the rate is cost of programming the machine as this is a relatively small cost that further diminishes as more preforms are laid up using the same program. L-preforms were laid up in pairs and took approximately 60 minutes and the U-preforms were laid up separately and took approximately 30 minutes.

3. *Hot draping cost* (AFP preforms only), which includes technician cost and consumables for vacuum bagging, as well as power consumption, maintenance, and depreciation of the oven. Similarly to the AFP estimations, all hourly rates are based on numbers from Heart Aerospace. The technician time accounted for 30 minutes of vacuum bagging L-preforms (per pair) and 20 minutes per U-preform. Each oven cycle was approximated to 70 minutes including 60 minutes of ramping up the temperature and 10 minutes rest at max temperature. The LU-style configuration does not account for an additional oven cycle for the U-preform as these shared the oven with the L-preforms.

4. *Adhesive cost*, was estimated using cost per square meter quoted by the manufacturer multiplied with the bonded area in each pi-joint configuration. As all other cost estimations, the adhesive cost was based on one meter of pi-joint, and he width of adhesive film was calculated as the perimeter length of the U-shaped clevis opening. Additionally, 30 minutes of technician time was accounted for all configurations to apply the adhesive film and vacuum bag the full panel.

As shown in Figure 6.16, the 3D woven pi-joint is the most expensive among the four pi-joint types, while the L-style and braided pi-joints are the most cost-effective options. It is important to note that the costs for both the 3D woven and braided

pi-joint preforms (fibres) are the quoted prices specific to this project and may vary based on supply available and order quantity. Note that all data is normalized since the exact values are proprietary information.

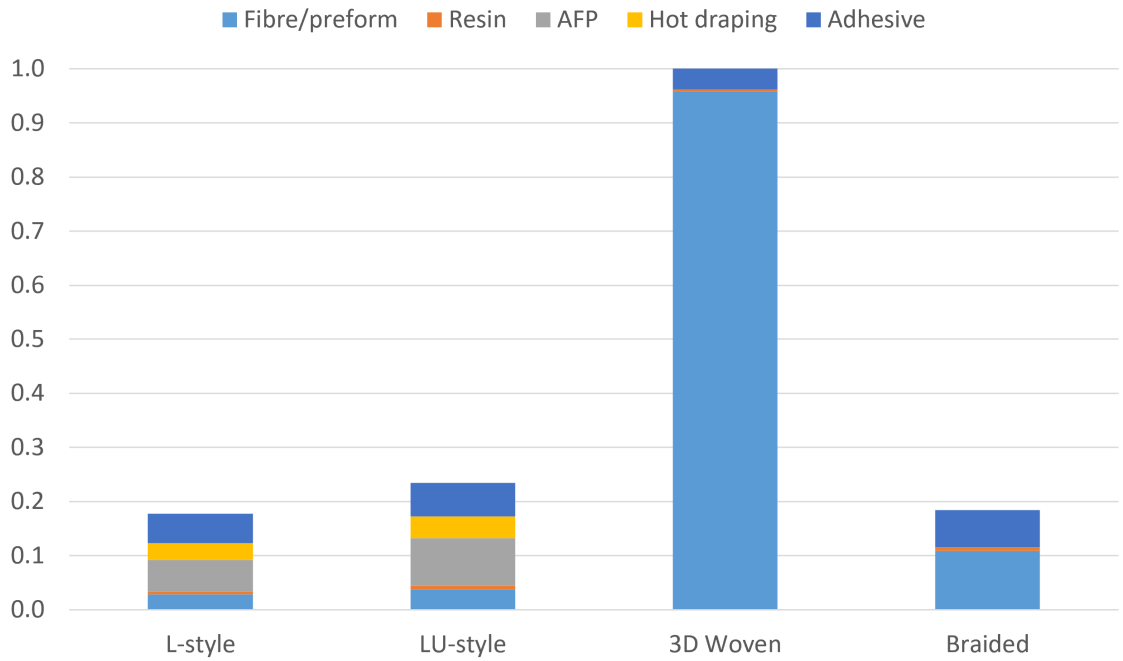

Figure 6.16: Normalized cost comparison of pi-joint configurations.

7

Conclusion

This chapter starts with presenting a brief summary of the thesis, followed by sections with conclusions drawn for each of the research questions. Additionally, the chapter ends with presenting future work for a continuation of the project.

In summary, four configurations of carbon composite pi-joints were investigated and prepared for physical testing. Two commercial pi-joints and two AFP preformed pi-joints, offering four configurations of different cost and manufacturing complexity. Resin infusion and bonding processes were developed to accommodate all four types of pi-joints with minimal differences to ensure consistent and comparable quality. A total of 64 test specimens were fabricated and quality checked for future pull-off and shear testing. Additionally, requirements for physical testing, including both fixture and specimen specifications, were defined to guide subsequent experimental work. In parallel, FE models were developed for each pi-joint configuration using justifiable simplifications to reduce the computational power required. These models aimed to predict the behaviours and failures of each pi-joint rather than their exact failure loads which would require more accurate material data. Lastly, three different NDI technologies were investigated, and compared on their performance on detecting defects in pi-joints and their scalability.

7.1 Comparison of pi-joint types

The first research question the project aimed to answer was “How do the four specified types of pi-joints compare to each other based on their strength, cost, and manufacturability?”. In Chapter 6 the four configurations of pi-joints were compared to each other in the three key areas separately, the following bar graph summarizes these comparisons to give a clear overview of the pros and cons of each configuration.

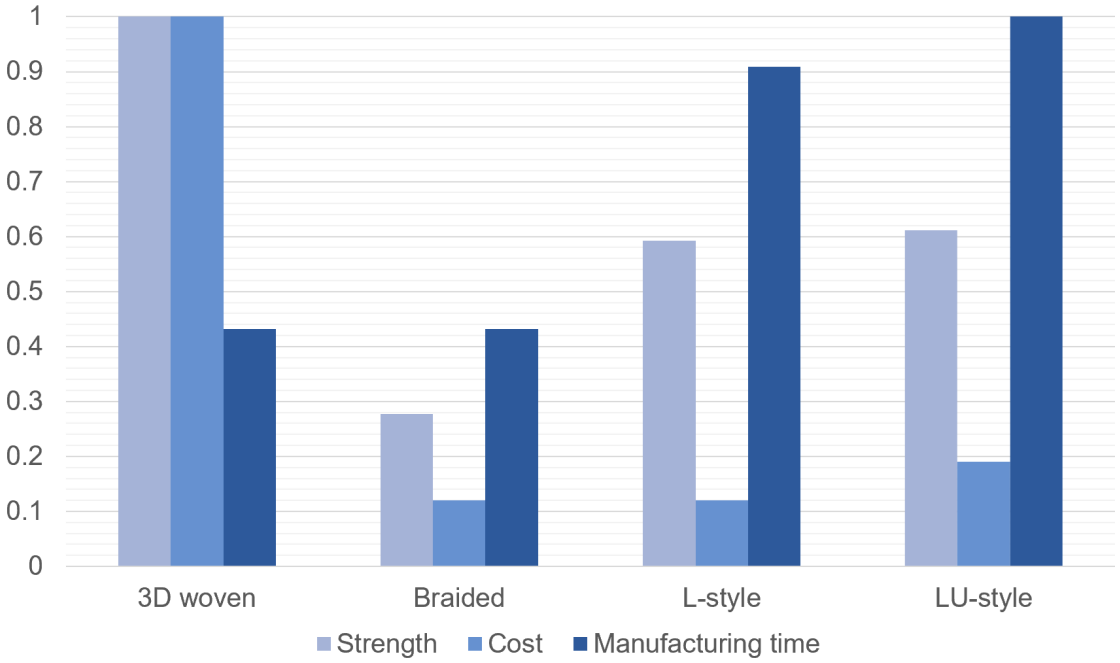

Figure 7.1: Overall comparison of the four pi-joint configurations in the three evaluated areas.

The 3D woven pi-joint offers excellent resin infusion characteristics, with its weave allowing resin to pass through much faster than the compacted HiTape UD fibres in the skin, making it ideal for large, single-shot infusions. It also conforms well to the web, resulting in a uniform bondline once the film adhesive is applied. However, it tended to ever so slightly warp inward during infusion, complicating the insertion of the web with film adhesive. This suggests it may be better suited for co-curing against the web rather than the skin, or that the bonding technique should be adapted to avoid this issue. Based on the predicted strengths from the FE models, the 3D woven pi-joint withstand significantly higher loads than the other configurations. Its greatest drawback is its high cost, between 5-10 times the cost of the other evaluated pi-joints.

The braided pi-joint stands out as one of the cheapest options with one of the lowest manufacturing times. Similarly to the 3D woven pi-joint, the braided fibres allow for good resin flow during infusions, reducing the risk of resin not reaching both sides of the joint when infused from a single side. Although not tested in this thesis, it should be noted that due to its braiding pattern, it is expected to offer improved crack resistance compared to the AFP preformed pi-joints. However, it has a significantly lower predicted strength than the other three configurations due to its thinner walls and base, especially in the root region. Another limitation is its susceptibility to fraying at the ends of the base and walls, unlike the 3D woven configuration where edges are continuously woven. This means it requires more careful handling during manufacturing to guarantee an even joint with the same properties along its entire length.

The L-style pi-joint introduces considerable manufacturing complexity and time due to the need for AFP layup and hot draping. While this adds flexibility since AFP machines can be used for various aircraft components, it can also become a bottleneck as the same machines are needed to layup other critical parts like wing skins which cannot be purchased off-the-shelf. Additionally, the low permeability of the hot-draped preforms resulted in much slower infusions than that of the off-the-shelf configurations increasing the risk of dry-spots or voids when used in larger structures. A key advantage of this pi-joint configuration is its adaptability, the joint's geometry can be tailored, such as varying thickness along its length, which is beneficial for optimizing material usage in for example an aircraft wing where the loads vary along its length.

The LU-style pi-joint as manufactured in this project closely resembles the L-style configuration in both structure and predicted performance. This project aimed to evaluate the AFP preformed pi-joints without additional filler material in the filler region. However, using carbon fibres as fillers could potentially have improved the conforming of the U-preform to the web during the infusions, assuring the fibres are better aligned with the load path through the joint.

7.2 Evaluation of NDI methods

The second research question aimed to answer was "How do the specified inspection methods compare to each other based on their ability to detect defects in pi-joints and scalability for use on entire aircraft wings?". Early in the project, thermography was excluded due to its relatively shallow inspection depth making in unsuited for inspecting pi-joints through the types of thick solid laminates used in this project. In contrast, ultrasonic pulse-echo showed more promising results, being able to detect defects in the base of the pi-joint from the bottom side of the skin laminate such as the missing tows and embedded flash tape. However, the inspection of the bondline quality is very poor as only the very bottom of the bond can be inspected and not the sides of the clevis itself. The X-ray CT-scan functioned well as a baseline as it could detect all three embedded defects, however due to the size limitations of inspection specimens it is not a scalable method for use on large aircraft structures. Therefore, neither of the evaluated NDI methods offer a complete solution to the problem at hand, and further investigation into other inspection methods would be required. Mainly focusing on methods to inspect the secondary bond from the outside of the skin.

7.3 FE modelling and validation

The last research question in the project was "How can the different types of pi-joints be modelled using FEA, and how well do these models predict the behaviour and failure?". Previous work on FE-modelling of complex composite joints shows that

a suitable modelling method for composite structures with significant out-of-plane forces are to use continuum shell elements interlaced with cohesive elements. Due to computational limitations in this project, the use of cohesive elements was focused to the interfaces between sub laminates, secondary bonded laminates, and resin-rich filler regions. Unfortunately, due to unforeseen delays in physical testing the FE-models could not be compared and evaluated against real physical test specimens.

7.4 Future work

The immediate continuation of this project is to physically test all the manufactured test specimens according to the test matrix presented in Subsection 5.3 to evaluate the FE models and get a better understanding of their exact failure modes. A few key components to increasing the precision of the FE models are more thorough material characterisation (including the cohesive properties), as well as implementing a progressive damage model such that a stiffness penalty is accounted for upon ply damage. With more computational power available there are multiple improvements to be made to the models such as finer mesh size and modelling cohesive interfaces between each ply of the L- and LU-style pi-joints, primarily in the corner radius.

Another area worth investigating further are potential improvements to the design and manufacturing of the L- and LU-style pi-joints, such as laying the fibres directly onto L-shaped tooling to avoid the hot-draping step. It could also be worth comparing the L- and LU-style pi-joints with and without carbon fibre fillers in the root region that minimise the resin-rich areas at the cost of an additional manufacturing step.

Lastly, the environmental conditions planned for physical testing are limited to varying temperature in dry conditions. However, as the different materials are affected differently by increased moisture, other failure modes can arise in conditions with high humidity which would be an important factor to investigate.

Bibliography

[1] B. Varughese A. Mukherjee. "Design guidelines for ply drop-off in laminated composite structures". In: *Composites Part B: Engineering* 32.2 (2001), pp. 153–164.

[2] A. Guelpa A. Plessis S. G. Roux. "Comparison of medical and industrial X-ray computed tomography for non-destructive testing". In: *Case Studies in Nondestructive Testing and Evaluation* 6 (2016), pp. 17–25.

[3] S. et al Abrate. "Cohesive zone models and impact damage predictions for composite structures". In: *Meccanica* (2015).

[4] A. Turon et al. "An engineering solution for mesh size effects in the simulation of delamination using cohesive zone models". In: *Engineering Fracture Mechanics* 74 (2007).

[5] F. Ciampa et al. "Recent Advances in Active Infrared Thermography for Non-Destructive Testing of Aerospace Components". In: *Sensors* 18 (2018).

[6] J. Jokinen et al. "The influence of the number of adhesive plies (FM 300-2) on fracture properties". In: (2021).

[7] J. Juan et al. "Void Content Minimization in Vacuum Infusion (VI) via Effective Degassing". In: *Polymers* 13.17 (2021).

[8] J. P. Kruth et al. "Computed tomography for dimensional merology". In: *CIRO Annals* 60.2 (2011), pp. 821–842.

[9] K. Verma et al. "Novel Design of Cocured 'T' Joints with Integrally Woven 3D Inserts". In: 2013.

[10] L. De Chiffre et al. "Industrial applications of cimouted tomography". In: *CIRO Annals* 63.2 (2014), pp. 655–677.

[11] L. Rui et al. "Evaluations on VCCT and CZM methods of delamination propagation simulation for composite specimens". In: *Aerospace Systems* 6 (2023).

[12] P. C. Paul et al. *Out of plane analysis for composite structures*. Tech. rep. NASA, 1990.

[13] P. Hallander et al. "An experimental study of mechanisms behind wrinkle development during forming of composite laminate". In: *Composites Part A: Applied Science and Manufacturing* 50 (2013), pp. 54–64.

[14] P. Potluri et al. *Influence of Fibre Architecture on Impact Damage Tolerance in 3D woven Composites*. 2012.

[15] R. Agogue et al. "Efficient Permeability Measurement and Numerical Simulation of the Resin Flow in Low Permeability Preform Fabricated by Automated Dry Fiber Placement". In: *Applied Composite Materials* 25 (2017), pp. 1169–1182.

[16] R. Harik et al. “Automated fiber placement defect identity cards: cause, anticipation, existence, significance, and progression”. In: *Proccedings of SAMPE 18*. 2018.

[17] W. Nsengiyumva et al. “Advances, limitations and prospects of nondestructive testing and evaluation of thick composites and sandwich structures: A state-of-the-art review”. In: *Composite Structures* 256 (2021).

[18] Y. Chung et al. “Detectability of Subsurface Defects in Polypropylene/Glass Fiber Composites Using Multiple Lock-In Frequency Modulated Algorithms”. In: *Applied Sciences* 13 (2022), p. 545.

[19] P. Middendorf B. Grisin S. Carosella. *Dry Fibre Placement: The Influence of Process Parameters on Mechanical Laminate Properties and Infusion Behaviour*. Tech. rep. Institute of Aircraft Design, University of Stuttgart, 2021.

[20] *Basic Prinicples of Ultrasonic Testing*. Last accessed 2nd of June 2025. URL: `https://www.nde-ed.org/NDETechniques/Ultrasonics/Introduction/description.xhtml`.

[21] L. J. Bond. “Fundamentals of Ultrasonic Inspection”. In: *Nondestructive Evaluation of Materials*. ASM International, 2018.

[22] C. C. Chamis. *Simplfied Procedures for Designing Composite Bolted Joints*. Tech. rep. NASA, 1988.

[23] Hexcel Corporation. *HexPly® 8552 Product Data Sheet*. 2023.

[24] Hexcel Corporation. *HiFlow® 1078-1 Product Data Sheet*. 2024.

[25] K. D. Potter D. H. J. A. Lukaszewicz C. Ward. “The engineering aspects of automated prepreg layup: History, present and future”. In: *Composites Part B: Engineering* 43.3 (2012), pp. 997–1009.

[26] A. Dacko. *Investigation of Finite Element (Fe) Modelling of Compsoite Materials: Shell, Solid and Solid Layered Composite Modelling - Comparison of Impact on Simulation Results*. Tech. rep. Warsaw University of Technology, Institute of Aeronatics and Applied Mechanics, 2020.

[27] *Data Presentation*. Last accessed 2nd of June 2025. URL: `https://www.nde-ed.org/NDETechniques/Ultrasonics/EquipmentTrans/DataPres.xhtml`.

[28] S. Hallström F. Stig. *Assessment of the mechanical properties of a new 3D woven fibre composite material*. Tech. rep. Royal Institute of Technology (KTH), 2009.

[29] S. Francis. “Aerospace pregpregs with braided reinforcement demonstrate improved production rates, cost”. In: *Composites World* (2025).

[30] Y. F. Gao and A. F. Bower. “A simple technique for avoiding convergence problems in finite element simulations of crack nucleation and growth on cohesive interfaces”. In: *Modelling Simul. Mater. Sci. Eng* 12 (2004).

[31] K.-T. Hsiao and D. Heider. “10 - Vacuum assisted resin transfer molding (VARTM) in polymer matrix composites”. In: *Manufacturing Techniques for Polymer Matrix Composites (PMCs)*. Ed. by Suresh G. Advani and Kuang-Ting Hsiao. Woodhead Publishing Series in Composites Science and Engineering. Woodhead Publishing, 2012, pp. 310–347.

[32] J. Summerscales I. R. Chowdhury. “Woven Fabrics for Composite Reinforcement: A Review”. In: *Advanced Composite Materials* 8.7 (2024).

[33] Altair Engineering Inc. *Cohesive Zone Modeling*. 2025.

[34] S. H. Ward J. B. Cushman S. F. McCleskey. *Design, Fabrication and Test of Graphite/Polyimide Composite Joints and Attachements, Summary*. Tech. rep. NASA, 1983.

[35] R. Kruger. "Development and application of benchmark examples for mixed-mode I/II quasi-static delamination propagation predictions". In: (2012).

[36] E. Lian. *Toray 3960/T1100GC 71E Gr 192 RC 33.5% 24K Uni-Directional Slit Tape (0.25 inch) Qualification Material Property Data Report*. Tech. rep. National Institute for Aviation Research, 2025.

[37] M. Dingeldein M. Bradley. *Advancements in braided materials technology*. Tech. rep. A&P Technology Inc, 2024.

[38] C. Soutis M. N. Saleh. "Recent advancements in mechanical characterisation of 3D woven composites". In: *Mechanics of Advanced Materials and Modern Processes* 3.12 (2017).

[39] G. Nehls. "Composite combat drone inlet duct proves novel fabrication approach". In: *Composites Wolrd* (2024).

[40] T. Ott. *Composite Hot Drape Forming*. Tech. rep. NASA, 1994.

[41] S. R. Hallett P. W. Harper. "Cohesive zone length in numerical simulations of composite delamination". In: *Engineering Fracture Mechanics* 75.16 (2008).

[42] A. Pirondi and F. Moroni. "12 - Simulating fatigue failure in bonded composite joints using a modified cohesive zone model". In: (2011), pp. 363–398.

[43] et al R. Kamiya. "Some recent advances in the fabrication and design of three-dimensional textile preforms: a review". In: *Mechanics of Advanced Materials and Modern Processes* 60.1 (2000), pp. 33–47.

[44] J. D. Russel. *Transitioning Advanced Aerospace Technologies through Cost and Risk Reduction*. Tech. rep. Air Force Research Laboratory Materials and Manufacturing Directorate Wright-Patterson Air Force Base, OH.

[45] Syensqo. *CYCOM® 5320-1 Product Data Sheet*. 2024.

[46] Syensqo. *FM® 300-2 Product Data Sheet*. 2024.

[47] A. P. Mouritz T. M. Koh S. Feih. *Experimental determination of the structural properties and strengthening mechanisms of z-pinned composite T-joints*. Tech. rep. School of Aerospace, Mechanical and Manufacturing Engineering, RMIT University, 2011.

[48] *User guide Abaqus: About Shell Elements*. Last accessed 31st of May. URL: https://docs.software.vt.edu/abaqusv2024/English/?show=SIMACAEELMRefMap/simaelm-c-shelloverview.htm.

[49] *User guide Altair Optistruct*. Last accessed 31st of May 2025. URL: https://help.altair.com/hwsolvers/os/topics/solvers/os/elements_user_guide_os.htm#reference_rp5_ltz_djb.

[50] L. Tsai X. Chen L. W. Taylor. "An overview on fabrication of three-dimensional woven textile preforms of composite". In: *Textile Research Journal* 81.9 (2011), pp. 932–944.

DEPARTMENT OF INDUSTRIAL AND MATERIAL SCIENCE
CHALMERS UNIVERSITY OF TECHNOLOGY
Gothenburg, Sweden
www.chalmers.se

CHALMERS
UNIVERSITY OF TECHNOLOGY